IS-T 1783

Submonolayer Nucleation and Growth and the Initial Stage of Multilayer Kinetic Roughening during Ag/Ag(100) Homoepitaxy

by

Zhang, Chenming

MS Thesis submitted to Iowa State University

Ames Laboratory, U.S. DOE

Iowa State University

Ames, Iowa 50011

Date Transmitted: August 1, 1996

PREPARED FOR THE U.S. DEPARTMENT OF ENERGY

UNDER CONTRACT NO. W-7405-Eng-82.

DISCLAIMER

This report has been reproduced directly from the best available copy.

AVAILABILITY:

To DOE and DOE contractors: Office of Scientific and Technical Information
P.O. Box 62
Oak Ridge, TN 37831

prices available from: (615) 576-8401
FTS: 626-8401

To the public: National Technical Information Service
U.S. Department of Commerce
5285 Port Royal Road
Springfield, VA 22161

TABLE OF CONTENTS

ABSTRACT

A comprehensive Scanning Tunneling Microscopy (STM) study of submonolayer nucleation and growth of 2D islands in Ag/Ag(100) homoepitaxy for temperature between 295K and 370K is presented. The initial stages of multilayer kinetic roughening is also studied. Analysis of an appropriate model for metal (100) homoepitaxy, produces estimates of 350 meV for the terrace diffusion barrier, 400 meV for the adatom bond energy, and 25 meV for the additional Ehrlich-Schwoebel step-edge barrier.

CHAPTER 1

GENERAL INTRODUCTION

1. The importance of thin film kinetics

Thin films are of importance from many aspects. Technologically, they are important because they have broad applications, such as optical coatings, corrosion protection, magnetic recording media, and semiconductor devices. Nucleation and growth processes are usually responsible for the structure of thin films grown on surfaces. Understanding the kinetics of film growth and finding out the parameters related to film developing are essential in developing methodologies of surface coating preparation. Critical size of islands, bonding energy between adatoms and the diffusion energy of adatoms are essential parameters in controlling the film growth. Thus the study of thin film kinetics and further the characteristic parameters associated with the film growth are important.

2. Film growth kinetics

2A. What happens when atoms hit the substrate surface? (from an atomic point of view)

When an atoms hit the substrate surface, it may experience different processes (Fig. 1). The adatom may be trapped at a special site on the surface, such as the step edge and defects, and it may also diffuse on the surface for a certain distance before it is trapped by a large island (growth), or meet another

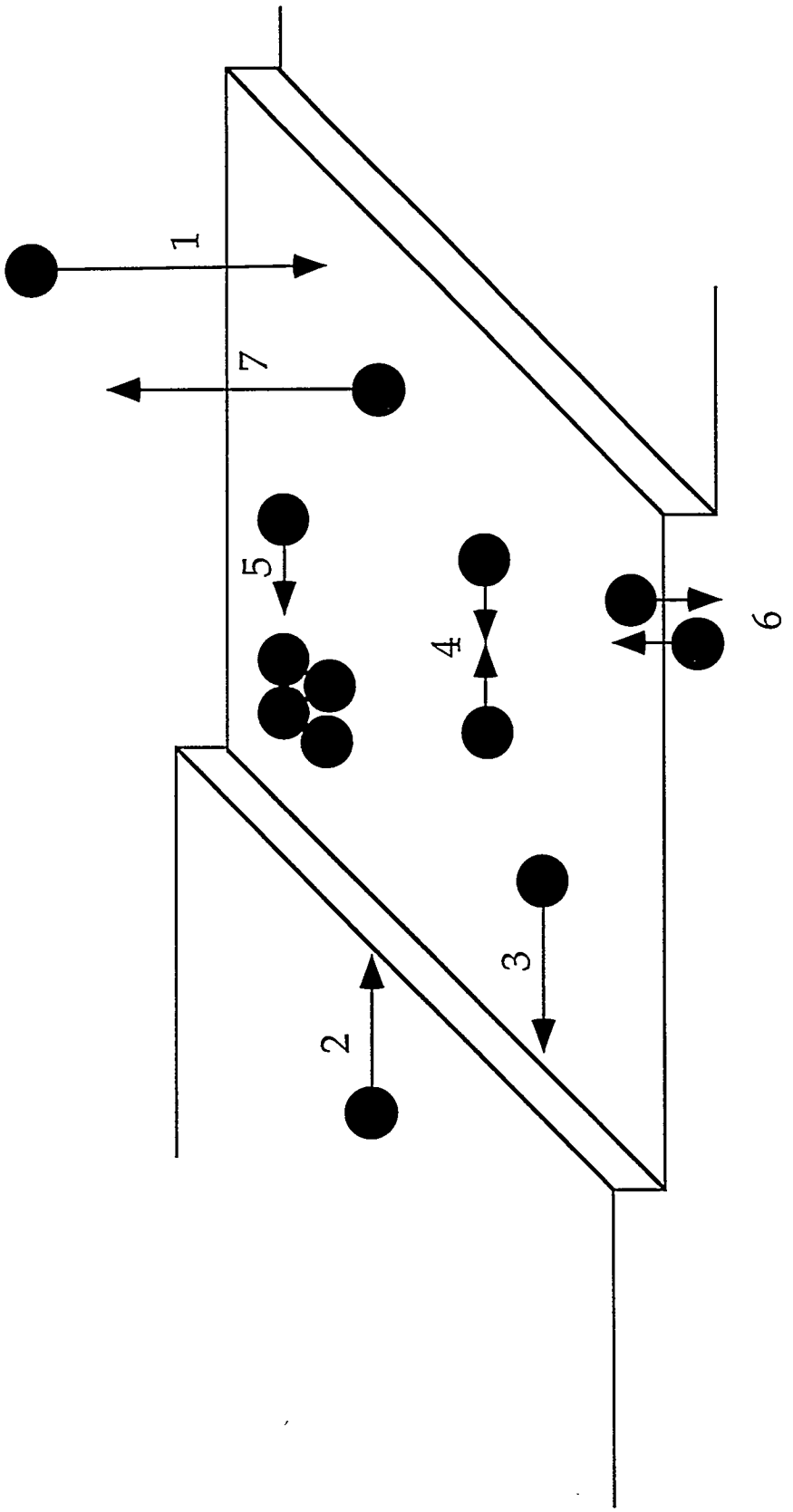
1
7
5
4
6
3
2

adatom or several other adatoms to form a new island (nucleation). It also may desorb and leave the surface to get into the gas phase, or diffuse into the substrate. For our interests, the surface diffusion and island formation are most important. Meanwhile, diffusion of adatoms and nucleation are characterized by the corresponding diffusion energy of adatoms and the binding energy between a pair of adatoms. Moreover, the island growth is characterized by the critical size of island, i, under certain condition (such as temperature). The critical size is a parameter which corresponds to the clusters with the lowest concentration, or highest free energy if equilibrium is assumed. In other words, i+1 is the size of a cluster which is more likely to grow than decay.

Concerning the energy, a terrace is by no means flat. The energies at the terrace edge are different from that on the terrace, and on the terrace, the energies at high coordinate sites (e.g. fourfold hollow lattice site (4fh)) are also different from those at low coordinate sites (e.g. 2-fold bridge sites) (Fig. 2). Obviously, adatoms need to surmount the surface diffusion energy to move from one adsorption site to another, and more energy will be needed to overcome the step-edge energy to "jump" down to another terrace.

2B. Different film growth models

Thin films can develop in different ways after adsorption on a surface through vapor deposition. To describe film structure, there are three classic thermodynamical film growth models as shown in Fig. 3. Thermodynamically, the driving force for adatoms to adopt different morphologies is to minimize the

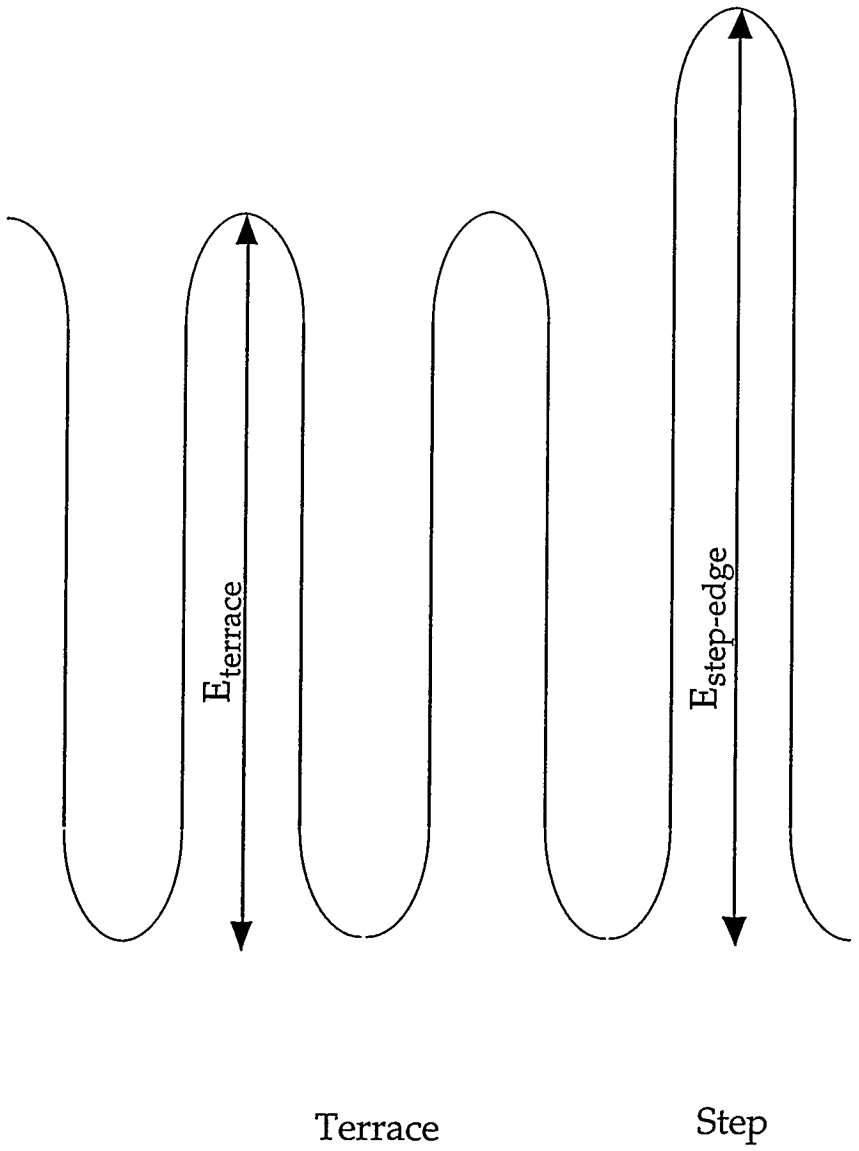

Figure 2. 2-D Surface potential energy

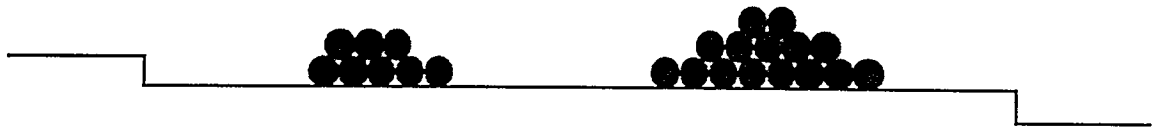

Volmer-Weber

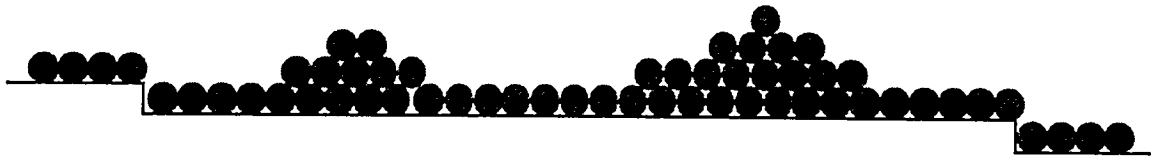

Stranski-Krastanov

Frank-van der Merwe

Figure 3. The three classic film grwoth models

surface energy. (1) When the following surface energy criteria is satisfied, i.e. $\gamma_f + \gamma_i > \gamma_s$, where γ_f, γ_i, and γ_s represents film, interfacial, and substrate energy respectively, the film growth will adopt Volmer-Weber growth model. (2) When initially $\gamma_f < \gamma_s$, Stranski-Krastanov growth model will prevail. In this case, layer growth dominates at the beginning. Then the interfacial energy, γ_i, increases with the thickness of the layer. The thermodynamic conditions for layer growth will be terminated after a certain layer thickness, and further growth will be dominated by more favorable island growth. (3) If $\gamma_f + \gamma_i < \gamma_s$, Frank-van der Merwe growth model will be followed. This is also called "layer-by-layer" growth.

For almost all homoepitaxial system, a layer-by-layer growth model is expected since the developing film is the same material as the substrate, for example, Ag/Ag [1], Pt/Pt [2], and Si/Si [3]. On the other hand, 3D island growth is more common in heteroepitaxial growth systems, such as metals on insulators and metals [4].

However, in practice, layer growth is never perfect. We might assume that a newly developed layer would not grow until the previous layer has been completed, but this never happens. In reality, a distribution of different heights over a terrace will be observed, and this is so-called surface roughness. This roughness depends not only on the diffusion of adatoms on the terraces, but also on the efficiency with which the adatoms can overcome other energy barriers, especially the barrier at the edge of the monolayer (ML) islands, and become incorporated at the edge of the growing ML-thick islands. If the adatoms could

diffuse for an unlimited time, the equilibrium state corresponding to Frank-van der Merwe, or layer-by-layer, growth would always be reached. However, it is kinetic factors which contribute to the surface roughness in many cases, but most obviously in heteroepitaxial systems.

During film growth, adatoms deposit onto the substrate at a certain rate (flux). After they land on the surface, they have a certain lifetime to diffuse on the surface before they are trapped by a potential well on the substrate, such as step edges, island edges, and defects, or combine with other adatoms to form 2D and even 3D islands. These kinetic factors lead to multilayer roughening in film growth, and this is also called as multilayer kinetic roughening.

Another thing that can happen is downward-funneling (DF) [5, 6]. This occurs because atoms that impinge on island edges, sides of microscopic pyramids, or other irregular features will "funnel downward" to the closest fourfold hollow (4fh) lattice site in a lower layer (see Fig. 4).

3. Literature review

In homoepitaxial growth, adatoms deposited on single crystal surfaces will diffuse across perfect terraces to interact with other adatoms and result in nucleation and growth of 2D islands [7,8]. Eventually, these islands will coalesce and form layers of films as growth proceeds further. Villain [9] has noted the instability in the evolution of surface morphology in systems where adatoms need more energy to overcome the activation barrier at island edges in downward transport than to diffuse on terraces. The extra activation barrier at

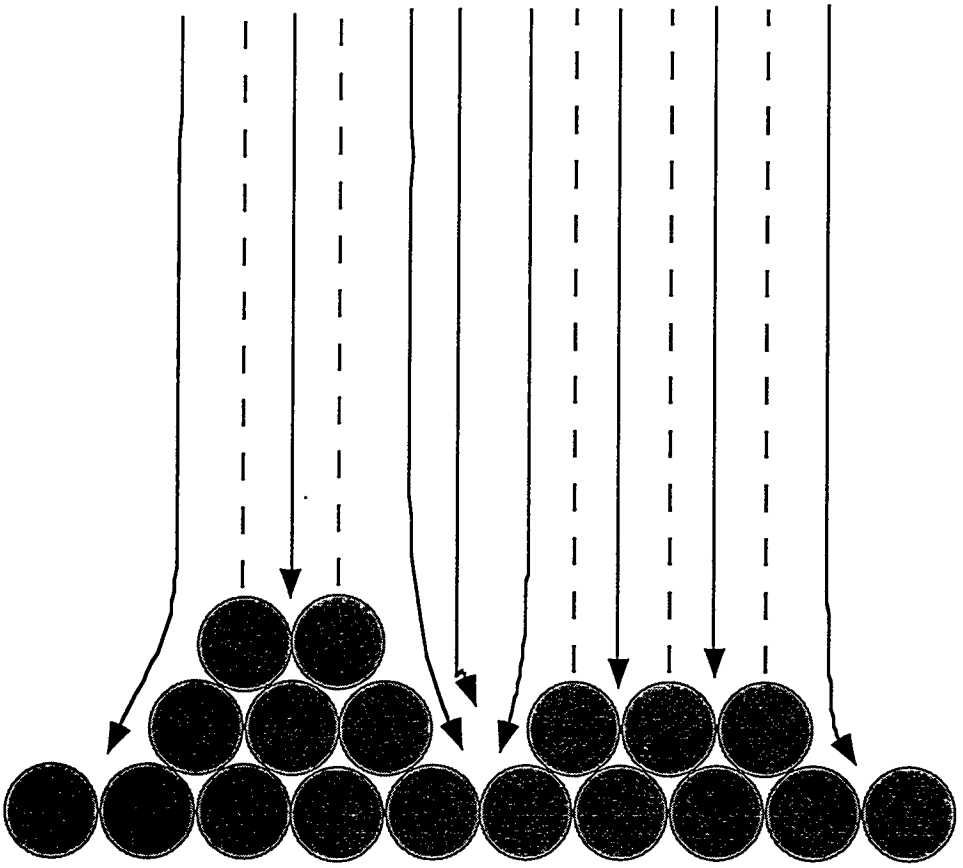

Figure 4. Downward funneling.

the step edge, so called Ehrlich-Schwoebel step-edge barrier (E_{sch}), which will prevent the diffusing atoms from transporting downward, is responsible for the instability.

Several metal on metal systems have been investigated either experimentally or theoretically to explore kinetic roughening. Meinel et al [10] investigated the growth of Au on Ag(111), Ag on Ag(111) and Ag on Au(111) by employing Auger Electron Spectroscopy (AES) and Transmission Electron Microscopy (TEM). They found that at perfect flat surfaces (mean step distance: 0.1-0.2 μm) and at temperature above 150°C, the film grows monolayer by monolayer via 2D nucleation. This is because at high temperatures, most of the adatoms can cross the step-edge energy barrier (E_{sch}) of the spreading islands. With falling temperatures, however, the jump probability becomes smaller, and the surface mobility of adatoms decreases. Consequently, 2D islands are formed on top of the underlying islands before the first monolayer can finish. This results in the formation of atomically stepped growth hillocks, and the hillocks become steeper with decreasing temperature.

It is certainly true that film growth will switch from layer by layer to 3D island growth with decreasing temperature, but it seems that this only happens in a certain range of temperature. Intensity oscillations in reflection high-energy electron diffraction (RHEED) [11] and in thermal-energy atom scattering (TEAS) [12] during epitaxial growth and ion sputtering are unique evidence for layer-by-layer growth and removal processes, respectively. TEAS [13, 14] and RHEED [15] experiments have been done at different temperatures in different metal-on-

metal system, and clear oscillations, evidence of layer-by-layer growth, have been observed. Comsa and his coworkers [16, 17] worked systematically on the growth of Pt on Pt(111) by TEAS and scanning tunneling microscopy (STM) over an extended temperature range (100-900 K). A gradual transition from the oscillatory to the nonoscillatory and eventually to the reentrant oscillatory behavior could be clearly shown by Fig. 5. It is believed that above 500 K the thermal energy of the adatoms is large enough so that they jump easily onto the layer below and there is no nucleation until layer completion. As the temperature decreases below 500 K the number of attempts for a successful jump becomes larger and so does the Pt adatom density on the islands, thus nuclei are formed on top of the islands, resulting in 3D growth and the disappearance of oscillations in Fig. 5. On the other hand, the reason for the reentrant 2D growth when the temperature is decreased further can be accredited to the reduced adatom mobility at lower temperature, which will result in reduced island size and/or less regular island shape. When island size is very small, and the retention of adatoms is small or even negligible [18], the adatoms may jump easily onto the lower level to complete the first monolayer growth before any stable cluster could form on the upper layer.

The kinetic roughening during homoepitaxial growth of GaAs(001) [19-22], Cu(001) [23, 24], Ge(001) [25], and Fe(001) [26] under certain conditions has also been studied. The roughening effect can be attributed to the existence of the extra energy barrier over step edges. Since atoms on an incomplete layer that recoil from this barrier are more likely to encounter one another, the probability for the

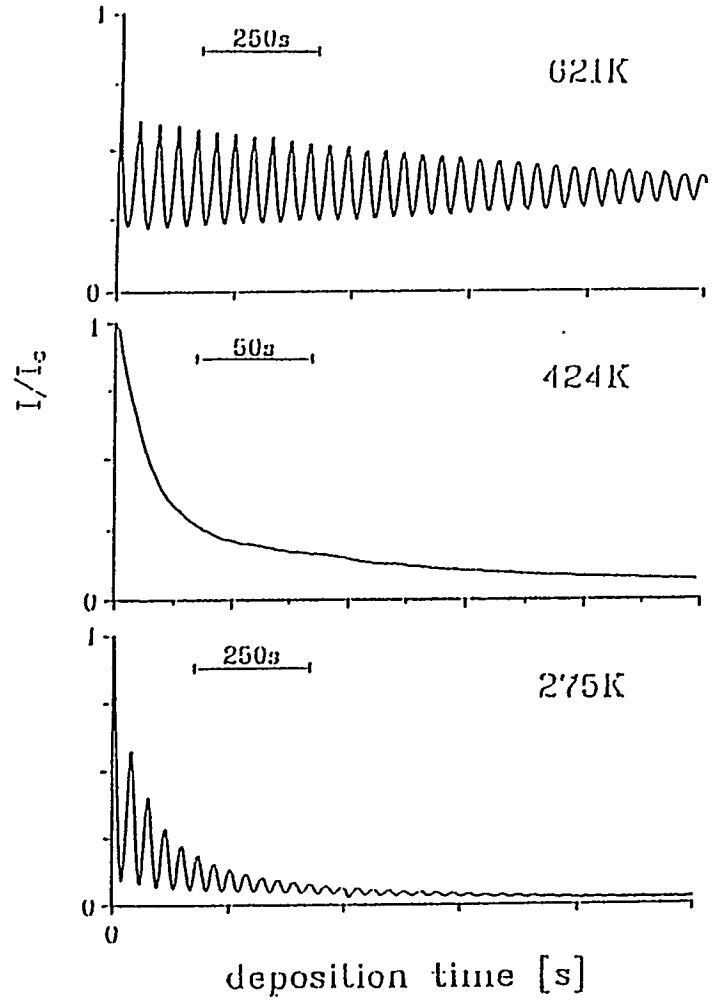

Figure 5. The normalized He specular peak height vs Pt on Pt (111) deposition time measured at three different surface temperatures [16]. The oscillatory behavior at high and low temperature is evidence for layer-by-layer growth; the monotonic decrease in the intermidiate region indicates 3D growth. (with permission)

nucleation of daughter islands (islands which develop on other islands) onto incomplete parent islands (islands which develop on substrate or on a previous completed film) is enhanced.

Bartelt and Evans [27] utilized computer simulations to provide the relationship between the surface roughness and temperature at fixed surface coverage (Fig. 6). Their simulations reveal the re-entrant phenomenon at lower temperature. They believe this is a consequence of the increase in the density of island edges resulting from the decrease in mean island size, and this will enhance the downward funneling effect to produce a smoother film.

Nevertheless, to better understand film growth mechanisms under different conditions, it is most crucial to find out the surface diffusion energy (E_d), Ehrlich-Schwoebel step-edge barrier (E_{sch}), and the characteristic binding energy between two adatoms (E_b). Many efforts have been made in this area. Fairly comprehensive data is available for homoepitaxial growth of Fe(100) [26, 28, 29] and Cu(100) [23, 30-32]. More limited data is currently available for Ni/Ni(100) [33], Pd/Pd(100) [34, 35], and Ag/Ag(100) homoepitaxy [36, 37]. Theoretical data are also available, and are summarized for Ag/Ag(100) homoepitaxy in Table III in Chapter 2.

It is the goal of this work to provide more accurate energy parameters for Ag/Ag(100) homoepitaxial system based on direct experimental results from STM.

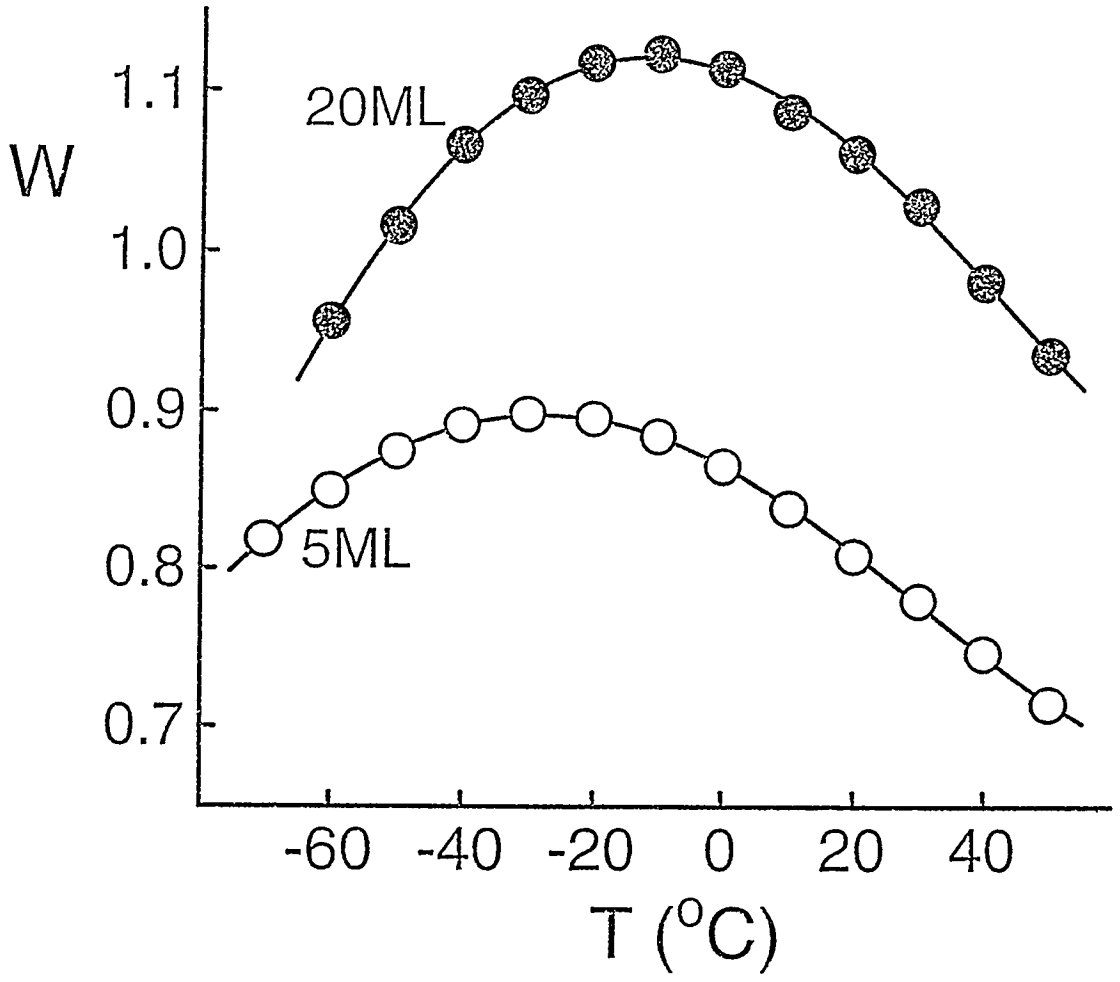

Figure 6. Simulation results for the variation of W with T at 5 ML and 20 ML [27]. Here W is the surface roughness factor, and a larger W value corresponding to a rougher surface. (with permission)

4. Experimental description

Because of its atomic resolution and the ability to scan relative large areas, STM has been an ideal tool in surface science studies. Its working principle and the methods adopted to isolate the STM system from vibration have been discussed elsewhere [38-43]. Only the most relevant experimental details will be discussed here.

4A. Chamber details

The whole STM sits in an ultra high vacuum (UHV) chamber which is attached to a main UHV chamber with a base pressure maintained below $1x10^{-10}$ Torr [38]. The main chamber is equipped with Auger Electron Spectroscopy (AES), Mass Spectrometer (MS), and Ion Bombardment Gun. Ag sample can be transferred from the main chamber to the STM chamber by a transfer rod.

The whole STM stage can be suspended in the chamber by a damped vibration isolation stage [38]. In order to scan over a large area (2100x2100 Å), the tunneling current is usually set up around 0.14 nA and the bias between the sample surface and the scanning tip is around 1.5 V. To obtain atomic resolutions, the tunneling current is set up around 0.14 nA and the bias around 0.005 V.

4B. Sample preparation

The Ag sample is aligned by Laue camera (X-ray diffraction) to less than 0.2 degree off the [100] normal. Then the sample is polished by using different grits of sand paper before using 1 μm and 0.25 μm diamond paste followed by silica colloid treatment. The alignment needs to be checked to make sure not much misalignment is introduced to the sample during the polishing process. Usually, the alignment should also be less than 0.4 degree off the [100] normal after polishing. Otherwise, the above processes need to be done again. Before putting the sample into the chamber, a thorough clean is needed with acetone and methanol and followed by hot air drying.

The Ag sample is first cleaned for about two weeks with cycles of ion bombardment for 30 minutes and annealing for another 30 minutes. The annealing temperature is increased from 323 K to 973 K with an increment of 50 K in order to thoroughly get rid of impurities, such as sulfur and carbon. AES is taken after each cleaning cycle to monitor the change of content of the impurities. If the AES signal of one impurity does not get smaller after a cycle, more cycles are needed with the same annealing temperature until the signal has been reduced significantly. Since the AES filament always spits some dirt onto the sample surface, AES is not done for a couple of days before a STM experiment.

4C. Sample description

With the alignment only 0.4 degree off the [100] normal, large terraces are not very difficult to locate if the sample is very clean. 2100x2100 Å scale terraces could be located every time, given enough time. However, some of our experiments were done on smaller terraces mostly because of the necessity to execute the experiment as quickly as we can.

Ag atoms are deposited onto the Ag sample by using a home-built Ag source. A block of silver is tightly wrapped with 0.5 mm diameter Ta wire, which acts as a heating resistor. This is not a perfect set up to mimic a molecular beam epitaxy (MBE) cell largely because consumption of the silver will change the power supply set up of the heating wire constantly. Calibration of the source needs to be done quite often in order to obtain wanted flux. However, relatively stable fluxes can be obtained if the consumption of silver is negligible. An improved MBE cell has been designed and built (see Appendix III) to provide stable fluxes, and experiments are being carried out to test its reliability.

5. Thesis organization

This thesis includes three chapters. Chapter 1 is a general introduction to the field of thin film growth. Chapter 2 is a paper entitled "Submonolayer nucleation and growth and the initial stages of multilayer kinetic roughening during Ag/Ag(100) homoepitaxy", which will be submitted to Surface Science. Chapter 3 discusses general conclusions regarding the work presented in Chapters 1 and 2. There are three appendices following Chapter 3. The

appendices contain additional work I conducted while at Iowa State University in the Department of Chemistry. Appendix I is a paper entitled "Oxygen adsorption on a single-grain, quasicrystal surface", which was published in Surface Science Volume 337 on page 135, 1995. Appendix II is a design of a new molecular beam source, and Appendix III is a summary of STM data for the work presented in Chapter 2.

References

1. J.-W. Wen, S.-L. Chang, J.W. Burnett, J.W. Evans, and P.A. Thiel, 73, 2591 (1994); J.-W. Wen, J.W. Evans, M.C. Bartelt, J.W. Burnett, and P.A. Thiel, Phys. Rev. Lett. 76, 652 (1996).

2. R. Kunkel, B. Poelsema, L.K. Verheij and G. Comsa, Phys. Rev. Lett. 65 (1990) 733.

3. Y.-W. Mo and M.G. Lagally, Surf. Sci. 248 (1991) 313.

4. J.A. Venables, D.J. Smith and J.M. Cowley, Surf. Sci. 181 (1987) 325.

5. Evens, J.W.; Sanders. D.E.; Thiel, P.A.; DePristo, A.E. Phys. Rev. 1990, B41, 5410.

6. Evans, J.W. Phys. Rev. 1991, B43, 3897.

7. J.A. Venables, Philos. Mag. 27, 697 (1973).

8. J.D. Weeks and G.H. Gilmer, Adv. Chem. Phys. 40, 157 (1979).

9. J. Villain, J. Phys. I (France) 1, 19 (1991).

10. K. Meinel, M. Klaua and H. Bethge, J. Crystal Growth 89, 447 (1988).

11. J.J. Harris, B.A. Joyce, and P.J. Dobson, Surf. Sci. 103, L90 (1981).

12. B. Poelsema, L.K. Verheij, and G. Cosma, Phys. Rev. Lett. 53, 2500 (1984).

13. L.J. Gomez, S. Bourgeal, J. Ibanez, and M. Salmeron, Phys. Rev. B 31, 255 (1985).

14. J.J. de Miguel, A. Sanchez, A. Cebollada, J.M. Callego, J. Ferron, and S. Ferrer, Surf. Sci. 189/190, 1062 (1987).

15. C. Koziol, G. Lilienkamp, and, E. Bauer, Appl. Phys. Lett. 51, 901 (1987).

16. R. Kunkel, B. Poelsema, L.K. Verheij, and G. Comsa, Phys. Rev. Lett. 65, 733 (1990).

17. M. Bott, T.Michely, and G. Comsa, Surf. Sci. 272, 161 (1992).

18. H.W. Fink and G. Ehrlich, Surf. Sci. 143, 125 (1984).

19. E.J. Heller and M.G. Lagally, Apply. Phys. Lett. 60, 2675 (1992).

20. C. Orme, M.D. Johnson, J.L. Sudijono, K.T. Leung, and B.G. Orr, Appl. Phys. Lett. 64, 860 (1994).

21. G.W. Smith, A.J. Pidduck, C.R. Whitehouse, J.L. Glasper, A.M. Keir, and C. Pickering, Appl. Phys. Lett. 59, 3282 (1991).

22. M.D. Johnson, C. Orme, A.w. Hunt, D. Graff, J.L. Sudijono, L.M. Sander, and B.G. Orr, Phys. Rev. Lett. 72, 116 (1994).

23. H.-J. Ernst, E. Fabre, R. Folkerts, and J.L. Lapujoulade, Phys. Rev. Lett. 72, 112 (1994).

24. H.-J. Ernst, E. Fabre, R. Folkerts, and, J.L. Lapujoulade, J. Vac. Sci. Technol. A 12, 1 (1994).

25. J.E. Van Nostrand, S.J. Chey, M.-A. Hasan, D.G. Cahill, and J.E. Greene, Phys. Rev. Lett. 74, 1127 (1995).

26. J.A. Stroscio, D.T. Pierce, M.D. Stiles, A. Zangwill, and L.M. Sander, Phys. Rev. Lett. 75, 4246 (1995).

27. M.C. Bartelt and J.W. Evans, Materials Research Society Proc. Vol. 399 (MRS, Pittsburgh, 1996).

28. J.A. Stroscio, D.T. Pierce, and R.A. Dragoset, Phys. Rev. Lett. 70, 3615 (1993).

29. J.A. Stroscio and D.T. Pierce, Phys. Rev. B 49, 8522 (1994).

30. H.J. Ernst, F. Fabre, and H. Lapujoulade, Phys. Rev. B 46, 1929 (1992).

31. J.-K. Zuo, J.F. Wendelken, H. Dürr, and C.-L. Liu, Phys. Rev. Lett. 72, 3064 (1994).

32. H. Dürr, J.F. Wendelken, and J.-K. Zuo, Surf. Sci. 328, L527 (1995).

33. E. Kopatzki, S. Günther, W. Nichtl-Pecher, and R.J. Behm, Surf. Sci. 284, 154 (1993).

34. D.K. Flynn-Sanders, J.W. Evans, and, P.A. Thiel, Surf. Sci. 289, 75 (1993).

35. D.K. Flynn-Sanders, J.W. Evans, and, P.A. Thiel, Surf. Sci. 298, 378 (1993).

36. Y. Suzuki, H. Kikuchi, and N. Koshizuka, Jap. J. Appl. Phys. 27 L1175 (1988).

37. P. Bedrossian, B. Poelsema, G. Rosenfeld, L.C. Jorritsma, N.N. Lipkin, and G. Comsa, Surf. Sci. 334, 1 (1995).

38. J.M. Wen, PhD thesis, Iowa State University, 1995.

39. J. Tersoff and D.R. Hamann, Phys. Rev. Lett. 50, 1998 (1983); Phys. Rev. B 32, 805 (1985).

40. C.J. Chen, J. Vac. Sci. Technol. A 6, 319 (1988); Phys. Rev. Lett. 65, 448 (1990).

41. N. D. Lang, Phys. Rev. Lett. 58, 45 (1987).

42. S. Ciraci, A. Baratoff, and I.P. Batra, Phys. Rev. B 41, 2763 (1990).

43. G. Doyen, and D. Drakova, Surf. Sci. 178, 375 (1986).

CHAPTER 2

SUBMONOLAYER NUCLEATION AND GROWTH AND THE INITIAL STAGES OF MULTILAYER KINETIC ROUGHENING DURING Ag(100) HOMOEPITAXY

A paper to be submitted to *Surface Science*

C.-M. Zhang, M.C. Bartelt, J.-M. Wen, J.W. Evans, C.J. Jenks, P.A. Thiel

ABSTRACT

We present results of a comprehensive Scanning Tunneling Microscopy study of Ag/Ag(100) homoepitaxy, for temperatures between 295 K and 370 K. This includes submonolayer nucleation and growth of two-dimensional islands and the initial stages of multilayer kinetic roughening. Comparison of observed behavior with results of Monte Carlo simulations of an appropriate model for metal(100) homoepitaxy, produces estimates of 330 ± 5 meV for the terrace diffusion barrier, 285 ± 10 meV for the adatom-adatom bond energy, and 25 ± 5 meV for the (additional) Ehrlich-Schwoebel step-edge barrier, assuming a common prefactor of 10^{12}/s.

1. Introduction

Metal(100) homoepitaxy [1-6] is usually initiated by submonolayer nucleation and growth of two-dimensional (2D) islands. At lower temperatures,

where island formation is irreversible, this process is controlled primarily by terrace diffusion. However, at higher temperatures, where bond-scission is operative, it is also dependent on adatom-adatom bonding [7]. Subsequently, island coalescence and nucleation of higher-layer islands lead to kinetic roughening of the multilayer film. The film roughness and morphology depend sensitively on (downward) interlayer transport, as well as on the submonolayer film structure. Downward transport involves both thermal diffusion of adatoms off island edges, which is typically limited by the presence of an Ehrlich-Schwoebel step-edge barrier [8], as well as "downward funneling" of depositing atoms from step edges and other microfacets to four-fold hollow adsorption sites [9].

Traditional analysis of submonolayer island nucleation and growth is cast in terms of a critical size, i, above which islands are effectively stable against dissociation [7]. Mean-field rate equations [7] then predict that the average island density, N_{av}, at fixed coverage, θ, satisfies

$$N_{av} \sim (R/\nu)^{\chi} \exp[E/(k_B T)], \quad \text{where } \chi = i/(i+2) \text{ and } E = \chi(E_d + E_i/i). \quad (1)$$

Here T is the surface temperature, R is the deposition flux (in monolayers per corresponding to the activation barrier E_d, and $E_i > 0$ is the binding energy for critical clusters of i adatoms ($E_1 = 0$). E_i is usually determined from the adatom-adatom bond energy, E_{bond}, within a simple nearest-neighbor bond-counting approximation. Using (1), measurement of the R-dependence of N_{av} determines

i, and measurement of the Arrhenius behavior of N_{av} determines E_d at low T where i=1, and then E_{bond} at higher T. Additional information is provided by the shape of the island size distribution. We note, however, that rarely is comprehensive and unambiguous data of the above type available. Also, second, ML/s), terrace diffusion occurs with hop rate $h=\nu\exp[-E_d/(k_BT)]$, refinement of this analysis may be required when i increases above unity, since there can be broad transition regions with increasing T between integral values of i [1,10,11]. For this reason, here we shall utilize a more precise and flexible analysis involving direct comparison of measured behavior with simulation results from a model of nucleation and growth which allows interpretation of data within those transition regions.

As noted above, the film roughness, and hence the full layer coverage distribution during multilayer growth, depend sensitively on the value of the Ehrlich-Schwoebel barrier, E_{Sch}. This barrier determines the reduced rate, $h'=\exp[-E_{Sch}/(k_BT)]h$, for an isolated adatom to diffuse down from an island edge (via bridge-hopping or place-exchange). The layer coverage distribution in the initial stages of multilayer growth can be estimated by combining an approximate diffusion equation analysis for adatom distributions on top of islands, together with appropriate nucleation theory for higher layer islands [12]. The boundary condition at the island edges naturally involves E_{Sch}, which can thus be estimated by comparing predictions against experimental observations [13]. A more precise approach extends the simulation studies for submonolayer growth [14] to the multilayer regime [15-17], including a step-edge barrier, E_{Sch}, and an

appropriate treatment of downward funneling [18]. Again, E_{Sch} is estimated by matching the experimental roughness, but the simulations can also be used to compare and analyze various other aspects of film morphology.

Fairly comprehensive data is available for Fe/Fe(100) [1] and Cu/Cu(100) [2] homoepitaxy, both for submonolayer nucleation and growth, and the subsequent multilayer kinetic roughening. More limited data is currently available for Ni/Ni(100) [3], Pd/Pd(100) [4], and Ag/Ag(100) homoepitaxy [5,6]. Ref.[11] summarizes known results for submonolayer behavior in these systems.

Here we present the first comprehensive Scanning Tunneling Microscopy (STM) study of submonolayer nucleation and growth for Ag/Ag(100) homoepitaxy between 295 K and 370 K, together with a study of the initial stages of multilayer growth. We analyze this behavior in order to produce reliable estimates of key energies, E_d, E_{bond}, and E_{Sch}. Previous studies examining submonolayer nucleation and growth in this system, with He-atom scattering [6], SPA-LEED [6,19,20], and surface X-ray scattering [21], provided only limited information on island separation behavior. These studies have not attempted to estimate key energies, E_d and E_{bond}, or to analyze critical size behavior. Smooth multilayer growth of Ag/Ag(100) was first indicated via diffracted intensity oscillations in RHEED studies for a broad range of T between 200 K and 400 K [5]. Such oscillations have also been seen, using a variety of other techniques [6,19-22], even as low as 80 K [20]. However, no quantitative analysis of this behavior has been performed to estimate the step-edge barrier, E_{Sch}, and only one recent study, using surface X-ray scattering, has attempted to precisely characterize the

kinetic roughening of the growing film [22]. Finally, we note one study of the "reverse process", i.e., of kinetic roughening during erosion of the Ag(100) surface, via Ar^+ ion-sputtering [23].

2. Experimental equipment and procedure

STM details, sample preparation, and sample description can be found in the experimental description in Chapter 1.

Measurement of the mean island density, N_{av}, and in some cases the full island size distribution, following deposition of 0.05-0.15 ML of Ag on Ag(100) was achieved by selecting and imaging a large (at least 1000x1000 $Å^2$) terrace on the sample. The STM images used for such analyses were obtained typically 15-60 minutes after deposition. By then, coarsening processes in the adlayer [24] have typically reduced the value of N_{av} by 5-15% since the end of deposition. In order to reliably estimate the N_{av} values immediately following deposition, we monitor the subsequent decrease of N_{av} with time, and then extrapolate back to the end of deposition. Only these latter values of N_{av} are reported here. A detailed analysis of the coarsening kinetics will be reported separately. We note that the statistical uncertainty, dN_{av}, in an estimate of N_{av} from an STM image containing M islands (with M ranging from 50 to 200 per sample) was determined using the relation $<(\delta M)^2> \approx 0.2M$ [25]. Final uncertainties in N_{av} do not exceed 10%.

Measurement of the layer coverage distribution, and thereby the film roughness, was performed after deposition of about 1 ML of Ag at 295 K. We

note that deviations from layer-by-layer growth are most apparent around monolayer coverages, so such data should provide the most sensitive estimates of the step-edge barrier. Since significant smoothing occurs before the first STM images can be obtained, we again monitor the subsequent evolution of the layer coverages (at fixed total coverage or film height) in order to reliably estimate their values immediately following deposition (via extrapolation, as above). Only the latter values are reported here. Results for the second layer island density after deposition of 1 ML of Ag are also reported. Again, this density is estimated by monitoring its decrease in time, and extrapolating back to the end of deposition.

3. Submonolayer nucleation and growth of 2D islands

Typical STM images, after deposition of about 0.1 ML of Ag, showing island distributions for various R at 295 K, are shown in Fig.1, and in Fig. 2 for various T with R≈0.06 ML/s. Quantitative analysis of such images is presented below. Note the typically square shape of the individual islands. This is a result of efficient island shape equilibration due to "rapid" diffusion of adatoms at island edges, as is characteristic of metal(100) homoepitaxy [1-3]. We exploit this (simplifying) feature in our modeling below.

3A. Experimental flux dependence of N_{av} at 295 K

Extensive data for N_{av} versus R, for R=0.001-0.1 ML/s, at 295 K, reveal scaling behavior of the form $N_{av} \sim R^{\chi}$, with $\chi \approx 0.30 \pm 0.02$. See Table I and Fig. 3.

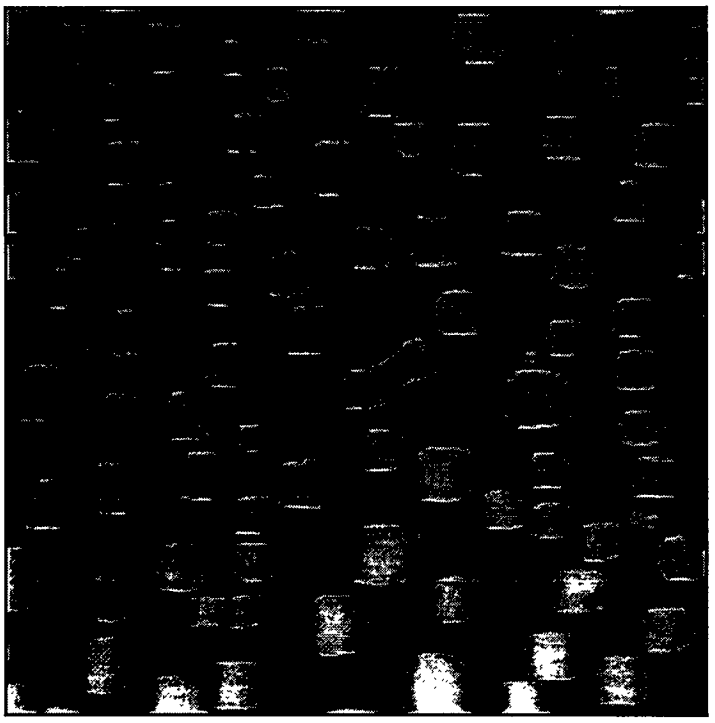

Flux = 0.0022 ML/s

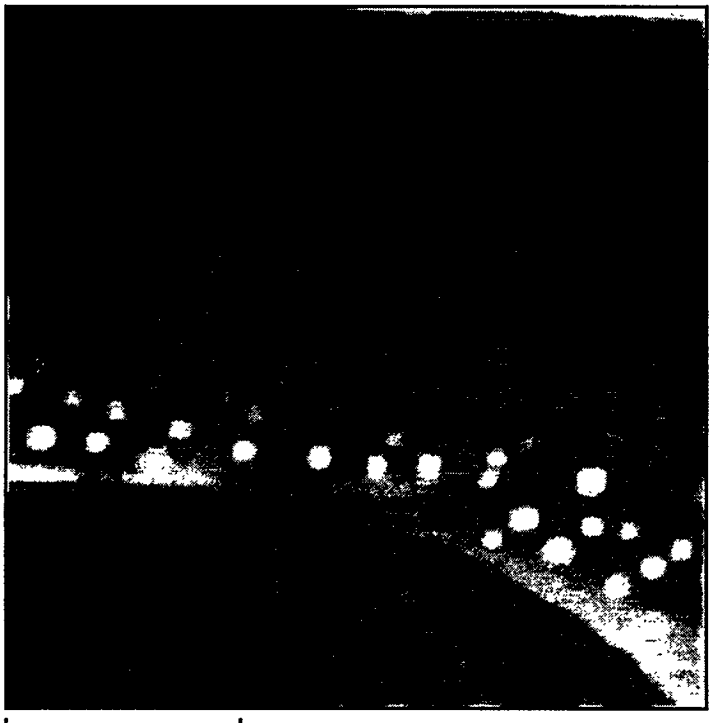

Flux = 0.0450 ML/s

500 Å

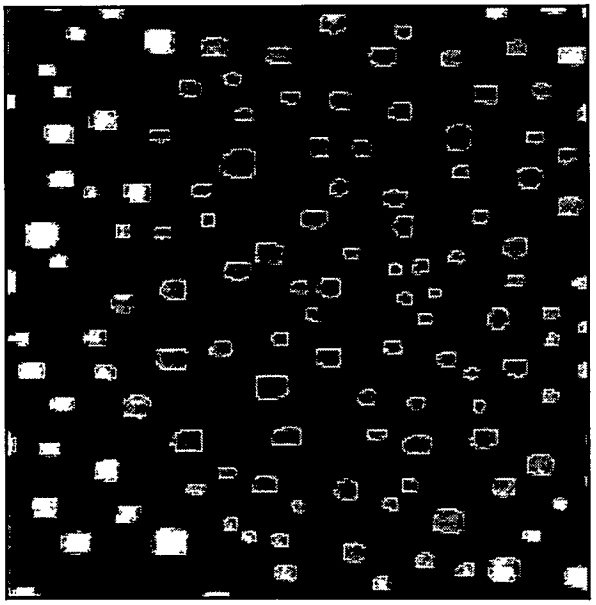

(a) T = 295 K

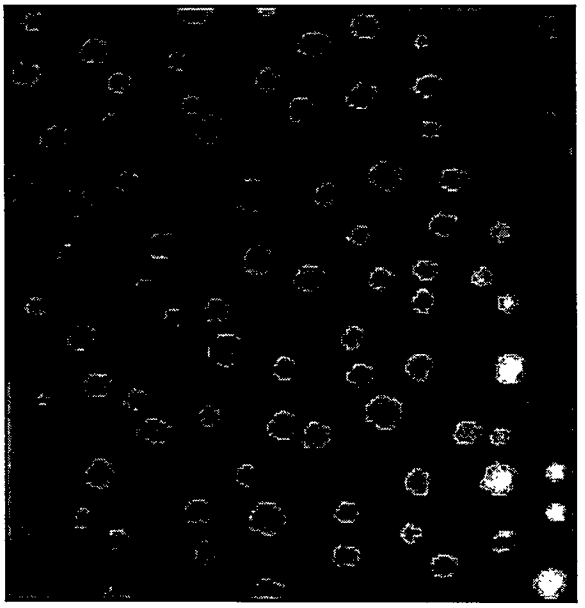

(b) T = 319 K, $\alpha = 120°$

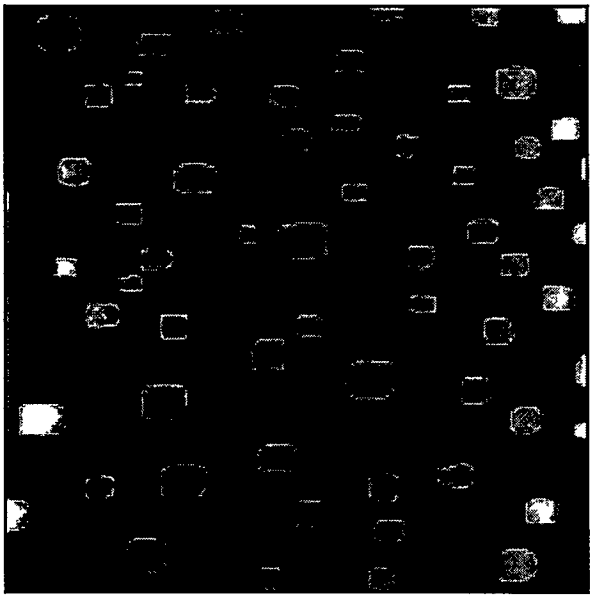

(c) T = 347 K

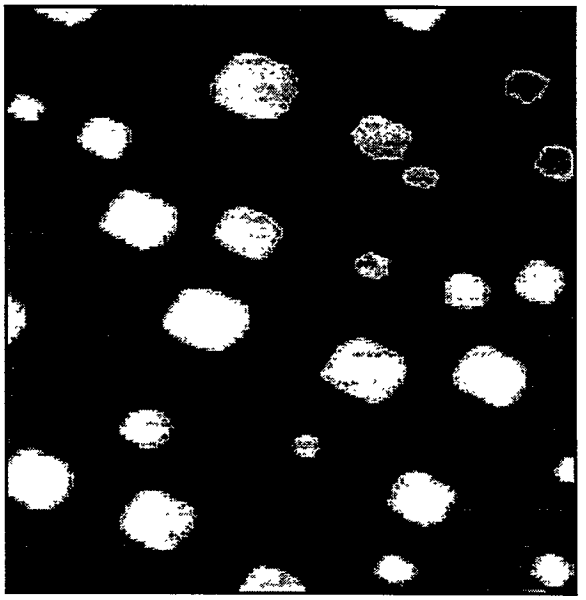

(d) T = 372 K, $\alpha = 30°$

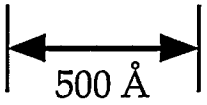

Constant Flux
Flux = 0.0625 ML/s

Table I- Experimental data for the flux dependence of N_{av} during Ag/Ag(100) homoepitaxy at 295 K. Coverages range between ~0.1 ML and ~0.25 ML. Normal and bold type data are from different samples. M is the total number of islands.

R($\times 10^{-2}$ ML/s)	N_{av}($\times 10^{-4}$ Å^{-2})	N_{av}($\times 10^{-4}$/site)	M
0.164	0.282	2.36	63
0.217	**0.363**	**3.04**	**126**
0.257	**0.414**	**3.46**	**104**
0.313	0.366	3.06	82
0.330	0.390	3.26	88
0.467	**0.463**	**3.87**	**139**
0.897	0.475	3.97	107
1.57	0.570	4.77	128
4.50	**0.964**	**8.06**	**194**
6.25	1.02	8.53	230
8.57	**1.04**	**8.70**	**417**

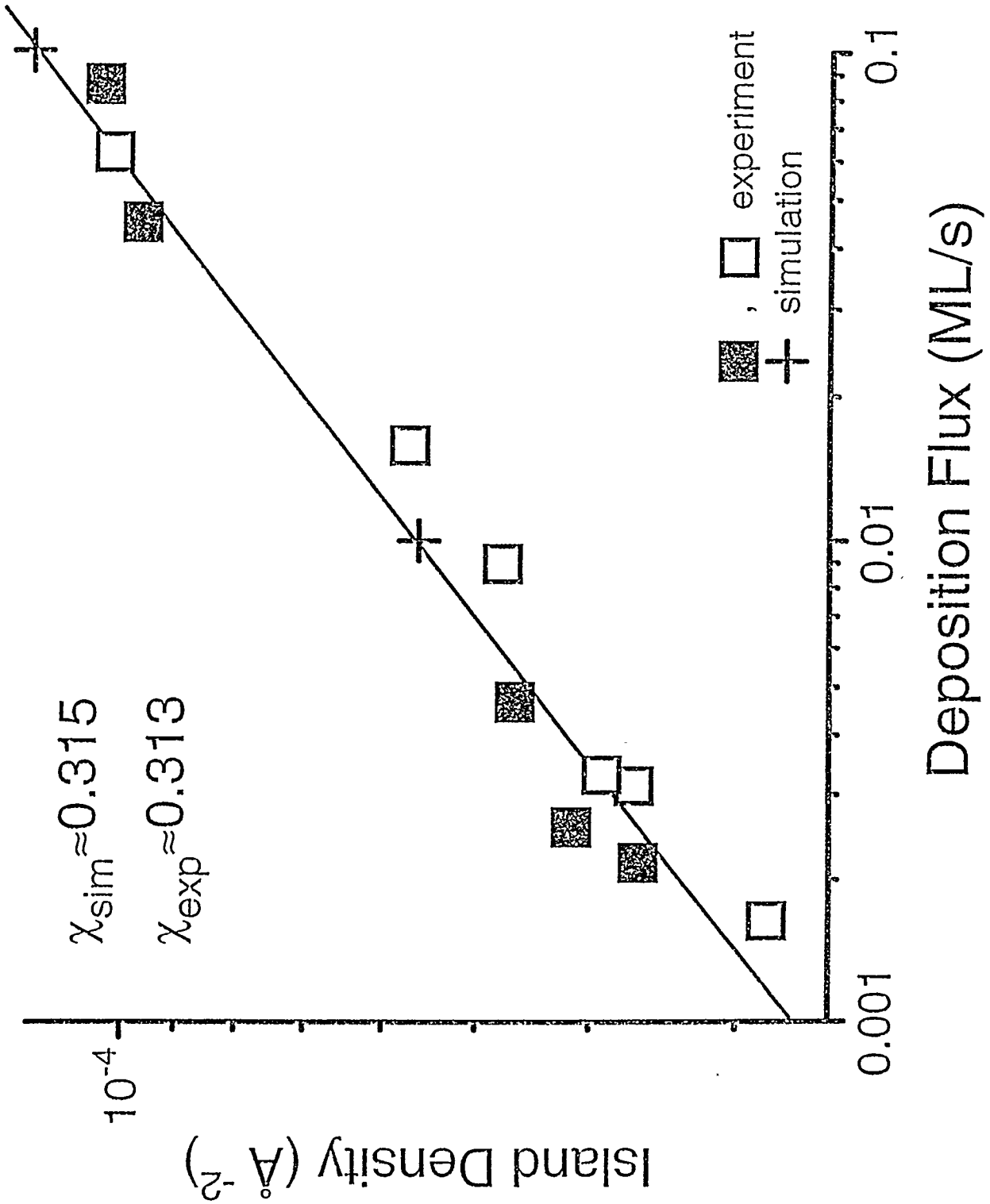
Island Density (Å -2)
10-4
χsim≈0.315
χexp≈0.313
0.001
0.01
0.1
Deposition Flux (ML/s)
, experiment
simulation

This effective value of χ provides strong indication of irreversible island formation (critical size i=1) at this temperature [26]. Note that for irreversible island formation, the value of χ is generally expected [14] to be somewhat below its classic "asymptotic" value of 1/3=0.333 [7]. We also note that in these determinations of N_{av}, the coverage varied between 0.05 ML and 0.15 ML. This variation does not complicate the analysis, since the island density is known to saturate at very low coverages (typically below 0.05 ML) during the nucleation and growth process, and to remain constant until island coalescence is significant (typically above 0.3 ML) [14].

3B. Experimental island size distribution at 295 K

The density, N_s, of islands of s atoms is naturally written as $N_s \approx \theta(s_{av})^{-2} f(s/s_{av})$, where $\theta=\sum sN_s$ is the coverage and $s_{av}=\theta/N_{av}$ is the average island size [14,27]. The normalized shape, f, of the island size distribution reflects the value of the island critical size [14,28], and more generally varies continuously in the temperature range where the system is making a transition between conventional integer critical sizes [10]. At 295 K, we expect near-"asymptotic" i=1 behavior in the experimental range of R (see also Appendix A), and therefore that f is basically independent of R. Thus we can combine N_s-data for different R, thereby reducing the statistical uncertainty to a reasonable level. The result for f shown in Fig. 4 is obtained from STM images taken 15-30 minutes after deposition. To properly compare with experiment, in the simulations we allowed for post-deposition incorporation of diffusing atoms into islands. This

Figure 4. Size distribution of Ag islands on Ag(100), formed at 295 K. Plotted is the scaling function f versus s/s_{av}. The bars are experimental data from analysis of STM images, with a total of 685 islands, and parameters in the range R=0.1-0.001 ML/s, θ=0.1-0.25 ML, and typical s_{av}=100-300 atoms. The lines are results from i=1 simulations of square islands with $E_{bond}=\infty$ and $h/R=10^9$ (i.e., $E_d\approx325$ meV, $\nu=10^{12}$/s, T=295 K, R=0.01 ML/s), correcting for post-deposition effects (dashed line) and for the STM finite resolution (solid line).

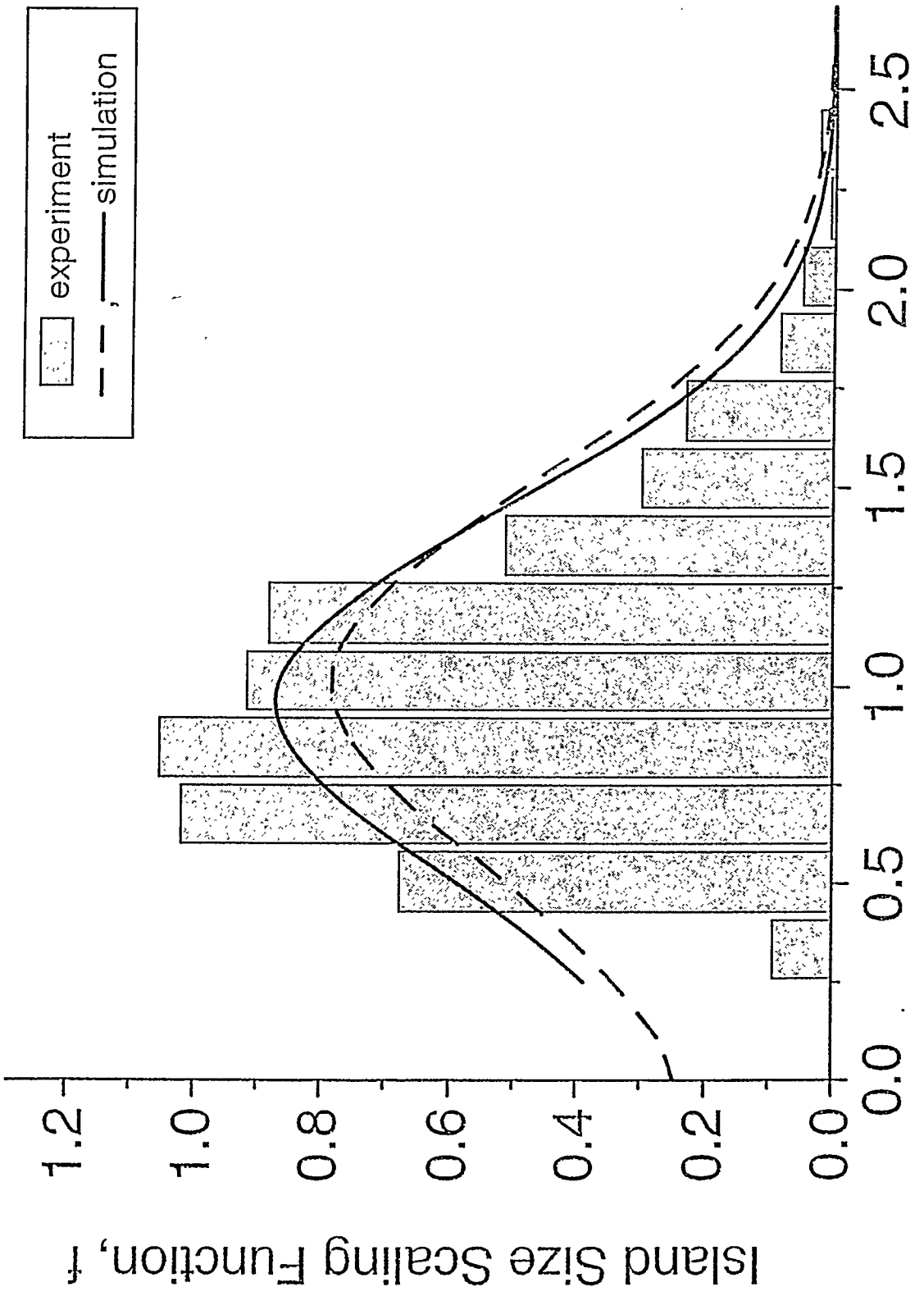
experiment
simulation
Island Size Scaling Function, f
1.2
1.0
0.8
0.6
0.4
0.2
0.0
0.0
0.5
1.0
1.5
2.0
2.5
S/S_av

modification lowers f, for small s, from the values at the end of deposition [14]. In addition, since the STM tip cannot detect (and could have ripened) very small islands, we introduced a small-s cutoff in the simulation N_s. Results are compared with experiment in Fig. 4 [26].

3C. Experimental arrhenius behavior of N_{av}

To examine the temperature dependence of the nucleation and growth process, we monitor the decrease in N_{av} with increasing T, from 295 K to 370 K, at (roughly) fixed $R \approx 0.06$ ML/s and (roughly) fixed $\theta \approx 0.1$ ML. See Table II. The corresponding Arrhenius plot is shown in Fig. 5. Clearly, the Arrhenius slope increases more-or-less continuously with increasing T above ~320 K, indicating the onset of reversible island formation. As an aside, we note that the upper limit on the experimental T-range is controlled by the need to have a statistically significant number of islands on the (broadest) terraces. An earlier RHEED study reported a transition to step-flow growth by 500 K [5], corresponding to an insignificant population of islands on terraces by this temperature.

3D. Analysis of the nucleation and growth process

For a simple first estimate of the terrace diffusion barrier, E_d, we exploit the experimental observation that island formation is effectively irreversible at 295 K. Thus we compare the observed island density, $N_{av} \approx 8.5 \times 10^{-4}$/site at 295 K for $R \approx 0.06$ ML/s and 0.1 ML, with that obtained from simulations of a model for irreversible nucleation and growth of square islands [14] in which the only free

Table II- Experimental data for the Arrhenius behavior of N_{av} during Ag/Ag(100) homoepitaxy. M is the total number of islands.

T(K)	R(ML/s)	θ(ML)	$N_{av}(\times 10^{-4}$ Å$^{-2})$	$N_{av}(\times 10^{-4}$/site)	M
295	0.0625	0.125	1.02	8.53	230
319	0.0550	0.110	0.769	6.43	173
347	0.0590	0.118	0.377	3.15	85
372	0.0720	0.144	0.106	0.887	24

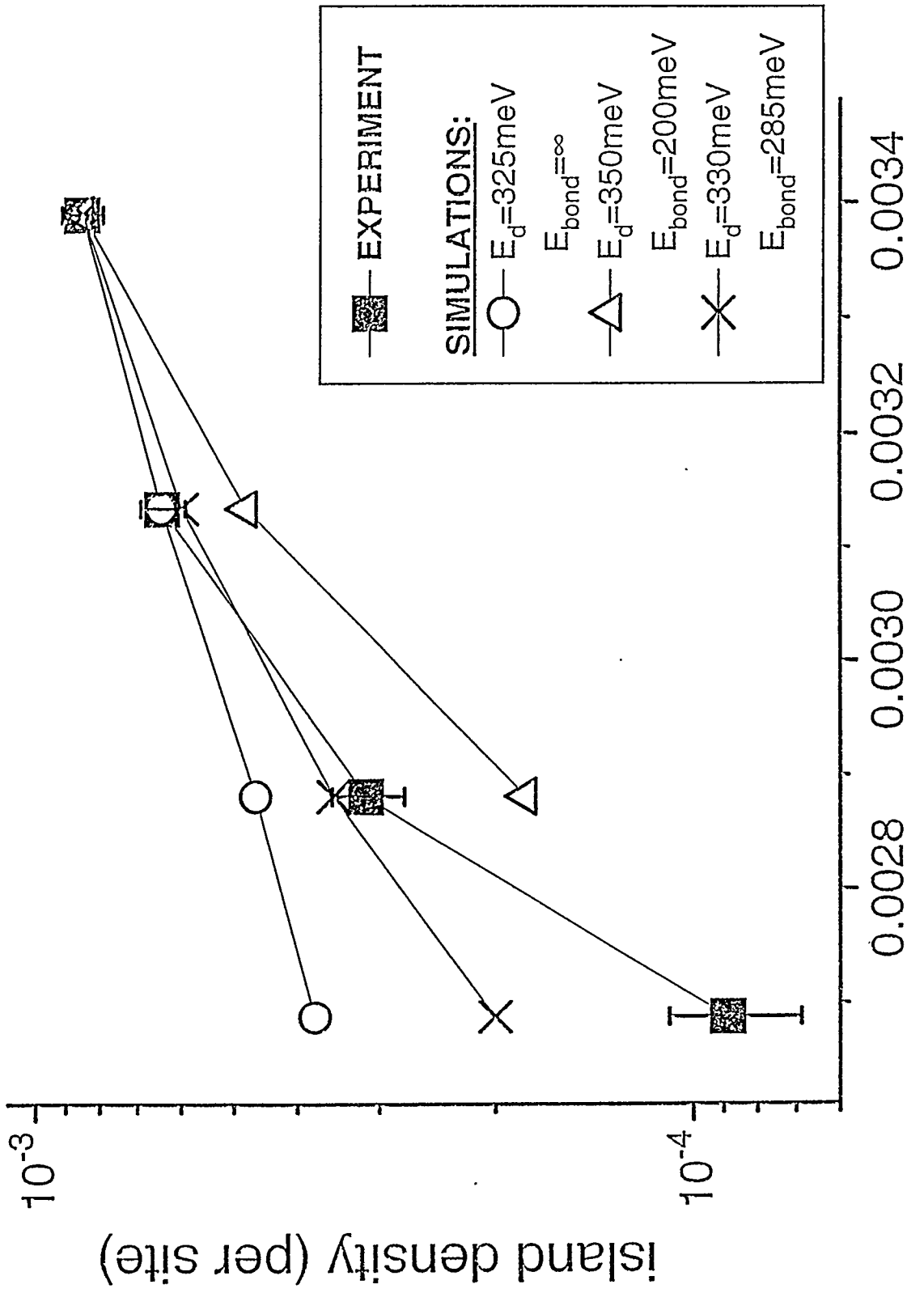
EXPERIMENT
SIMULATIONS:
E_d=325meV
E_{bond}=∞
E_d=350meV
E_{bond}=200meV
E_d=330meV
E_{bond}=285meV
island density (per site)
10^{-3}
10^{-4}
0.0028
0.0030
0.0032
0.0034
1/T (K^{-1})

parameter is the hop rate, h, for terrace diffusion. To match N_{av} with this model, we need $h \approx 2.8 \times 10^6$/s at 295 K, so $E_d \approx 325$ meV assuming $\nu \approx 10^{12}$/s. This value of E_d is consistent with the experimental Arrhenius slope of 100 meV$\approx \chi E_d$ for N_{av} at 295 K (Fig. 5) using the experimental $\chi \approx 0.313$. The model also predicts that $\chi \approx 0.315$ (Fig. 3), for the same parameters, again consistent with experiment.

Clearly, one must account for reversible island formation to describe the increasing Arrhenius slope of N_{av} above ~320 K (Fig.5). In fact, the above analysis assuming irreversible island formation ($E_{bond}=\infty$) can be regarded as providing a strict lower bound on E_d. Indeed, if island formation is reversible ($E_{bond}<\infty$), then island nucleation is more difficult, which would tend to lower N_{av}. In order to compensate and recover the observed value of N_{av}, terrace diffusion must be reduced (i.e., E_d increased).

To analyze the observed Arrhenius behavior, we utilize simulations for nucleation and growth of square islands including single adatom-adatom bond scission at rate $\exp[-E_{bond}/(k_BT)]h$, and double bond scission at rate $\exp[-2E_{bond}/(k_BT)]h$. We first match the observed N_{av} at 295 K for $R \approx 0.06$ ML/s, which uniquely determines the value of E_{bond} for each chosen $E_d \geq 325$ meV [29]. For example, choosing $E_d=330$ meV yields $E_{bond}=285$ meV, $E_d=340$ meV yields $E_{bond}=250$ meV, $E_d=350$ meV yields $E_{bond}=230$ meV, etc.. Examining the predictions of the model, with such pairs of energies, for the Arrhenius behavior of N_{av}, we find that the experimental data is best fit by the choice of $E_d \approx 330$ meV and $E_{bond} \approx 285$ meV. Higher (lower) values of E_{bond} produce a too slow (too rapid) decrease in N_{av} with increasing T. See Fig. 5. In Fig. 6 we show typical

Figure 6. Adlayer configurations obtained in the simulations on a 1000×1000 Å^2 lattice, for E_d=330 meV, E_{bond}=285 meV and $\nu=10^{12}$/s. In

(a) T=295 K; R=4.5×10^{-2} ML/s and θ=0.1 ML (a1); and R=3.3×10^{-3} ML/s θ=0.25 ML (a2).

(b) θ=0.1 ML, R=0.06 ML/s, and, from (b1) to (b4), T=295 K, T=319 K, T=347 K, and T=372 K.

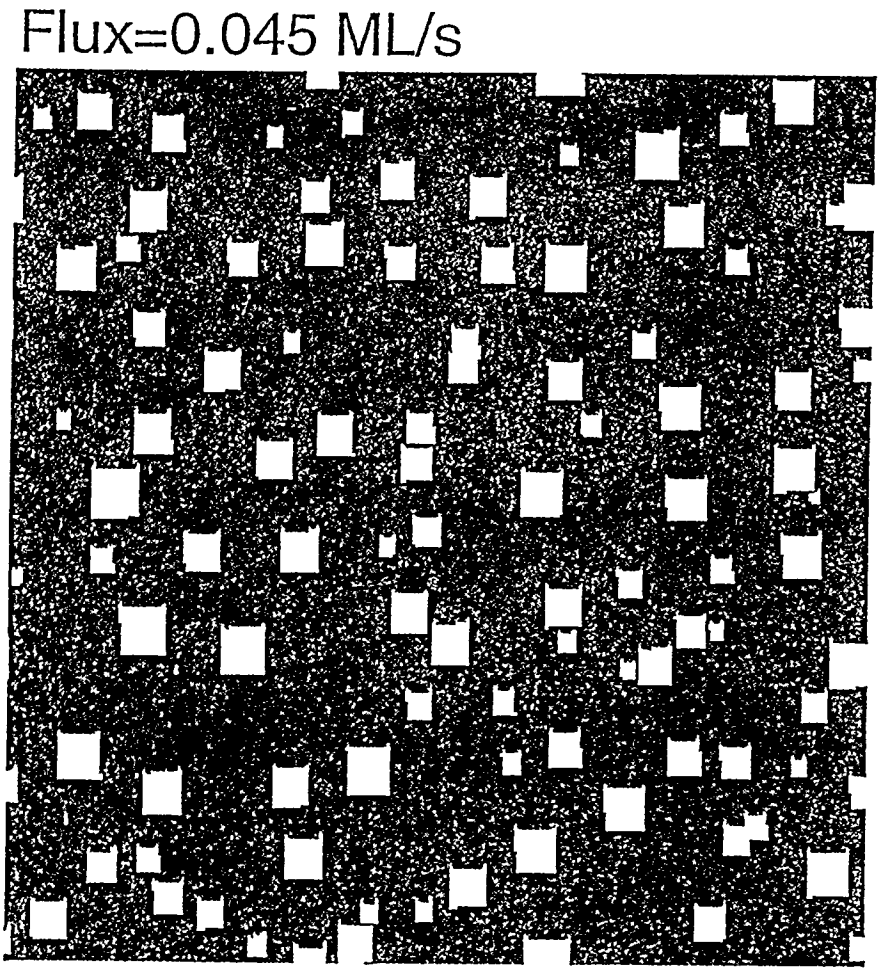

Fig. 6. (a1)

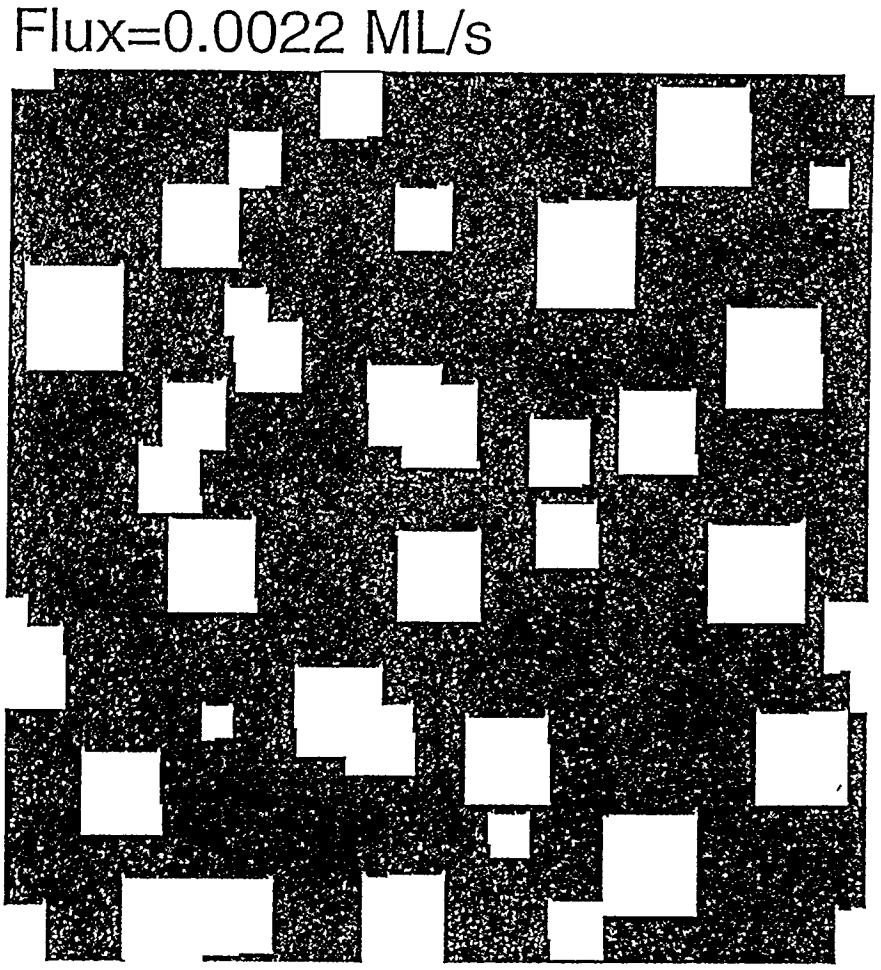

Fig. 6. (a2)

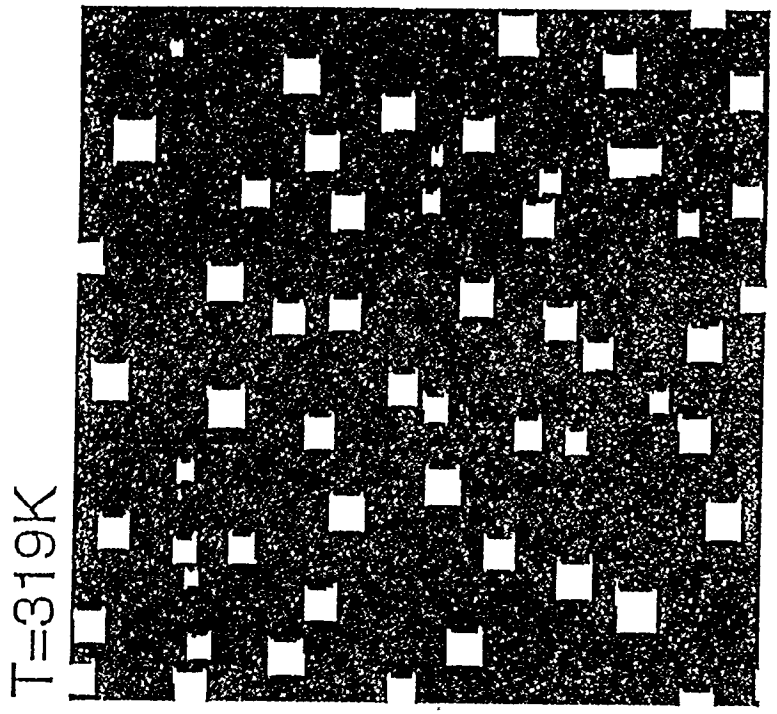

Fig. 6. (b2)

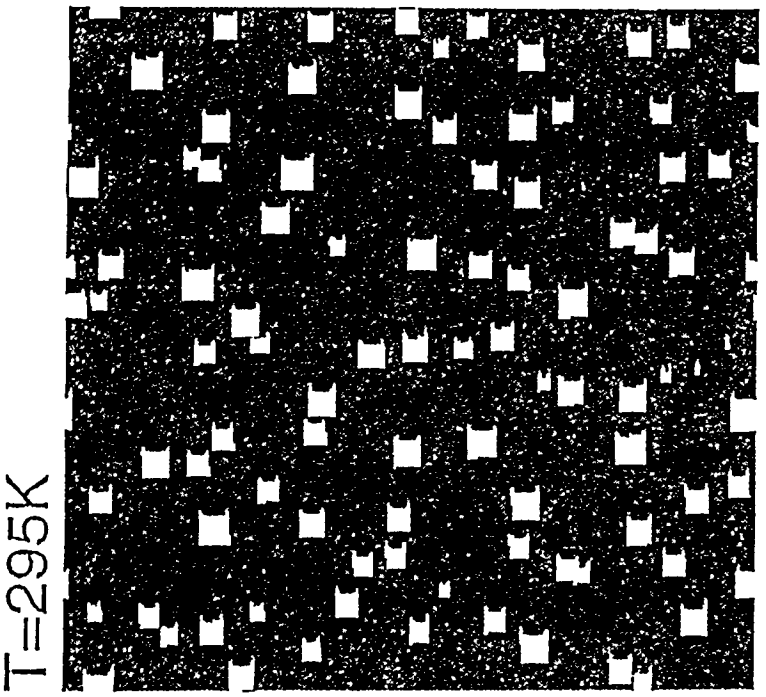

Fig. 6. (b1)

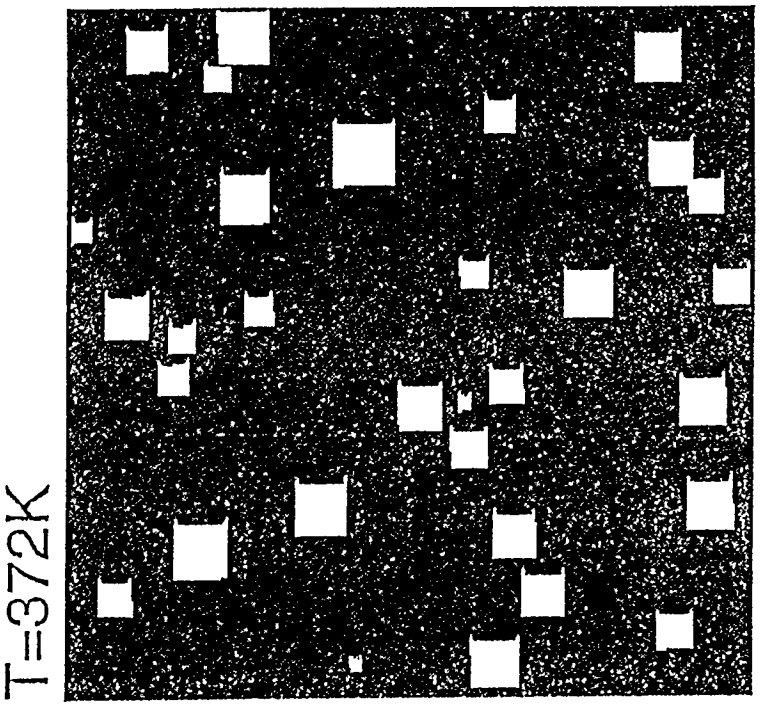

Fig. 6. (b4)

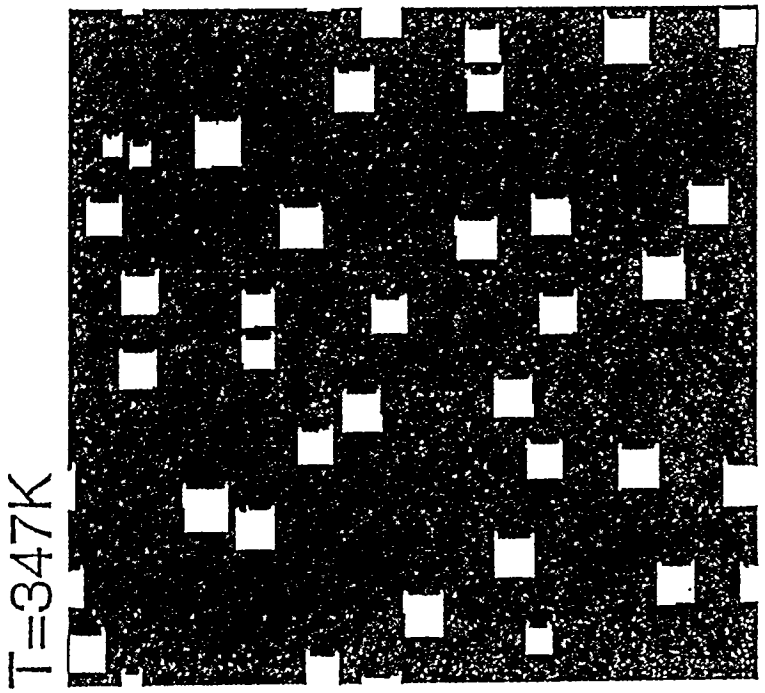

Fig. 6. (b3)

adlayer configurations obtained in the simulations with these parameters, for the R, T, and θ chosen as in Figs. 1 and 2.

We note that our model enforces the (near) square "equilibrium" island shape by instantaneously incorporating each aggregating adatom at the kink site of the growing island. Thus we suppress fluctuations in island shape, specifically excluding the possibility of having singly-bonded adatoms at island edges (except for certain island configurations, such as trimers, pentamers, septamers, etc.). Since we thereby underestimate the number of kink sites, we somewhat underestimate the total island dissociation rate. However, we do correctly treat dissociation of dimers which is the primary factor in determining N_{av} behavior in the temperature range considered. Also, note that dissociation-recondensation events tend to naturally suppress the kink density at island edges (by providing an additional pathway for efficient edge diffusion [10]). Thus our reported E_{bond} presumably only slightly underestimates the actual value.

It is instructive to note that for $E_d \approx 330$ meV and $E_{bond} \approx 285$ meV (and $R \approx 0.06$ ML/s), the simple criteria presented in [11], and refined in Appendix A, indicate that the regime of i=1 should extend up to the temperature $T_{1+} \approx 300$ K, a crossover regime from i=1 to i=3 should extend from T_{1+} to $T_{3-} \approx 370$ K, and the i=3 regime should extend from T_{3-} to $T_{3+} \approx 390$ K, above which double-bond scission becomes significant, and behavior does not correspond to a well-defined integer i [10,11]. These predictions are in fairly good agreement with the observed Arrhenius behavior (Fig. 5).

Finally, for comparison with our estimate, in Table III we list previous theoretical predictions for E_d, for both the bridge-hopping (hop) and place-exchange (exch) mechanisms. Our analysis of the experimental data always selects the lowest barrier, which theory indicates is for bridge-hopping. We have also listed theoretical estimates for E_{bond}. We believe that our experimental estimates for E_d and E_{bond} are considerably more reliable than the most sophisticated theoretical estimates currently available.

4. Multilayer growth

Our multilayer growth studies were performed only at 295 K, with fixed $R \approx 0.055$ ML/s. Typical STM images obtained 45-60 minutes after deposition of 1 ML of Ag are shown in Fig. 7. It should be noted that although the layer coverages have only changed slightly from their values immediately following deposition, some features of the morphology have changed dramatically. For example, immediately after deposition, the vacancies remaining in the incomplete fist layer are expected to have rather irregular shapes [15]. However, in the image shown in Fig. 7, these have radically restructured to achieve more compact (near-square) shapes.

Below, θ_j will denote the coverage of layer j=1,2,.., with j=0 corresponding to the top substrate layer (so $\theta_0=1$, and $\theta=\theta_1+\theta_2+...$).

Table III- Estimates of E_d and E_{bond} (in meV) for Ag/Ag(100), from Embedded Atom (EA), Effective Medium (EM), Morse potentials (MP), and *ab initio* calculations. The last row shows our estimates.

METHOD	E_d (hop)	E_d (exch)	E_{bond}
EAM-VC[a]	480	600	280
EAM-AFW[a]	480	750	-
MD/MC-CEM[b]	460	700	350
CEM[b]	400	410	-
EMT[c]	365	-	191
MP[d]	400	-	-
1st PRINCIPLES[e]	500	-	-
THIS WORK	330±5	-	285±10

[a] C.-L. Liu, J.M. Cohen, J.B. Adams, and A.F. Voter, Surf. Sci. **253**, 344 (1991).

[b] L.S. Perkins and A.E. DePristo, Surf. Sci. **325**, 169 (1995).

[c] P. Stoltze, J. Phys. Condens. Matter **6**, 9495 (1994).

[d] Ref.[23].

[e] G. Boisvert, L.J. Lewis, M.J. Puska, and R.M. Nieminen, Phys. Rev. B **52**, 9078 (1995); P. Ruggerone, B.-D. Yu, C. Ratsch, and M. Scheffler, Bull. Am. Phys. Soc. **41**, 631 (1996).

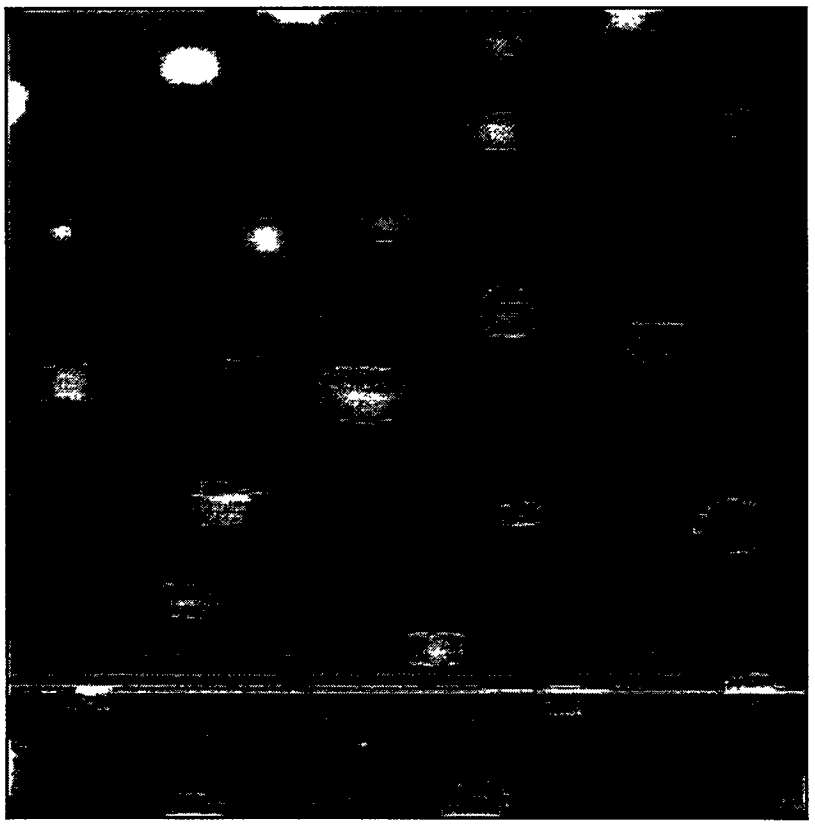

Figure 7. STM image (1500×1500 Å^2) of Ag/Ag (100), obtained with R≈0.055 ML/s, at 295 K, approximately 45 minutes after deposition. Darker regions have lower height. Coverages (in ML) are $\theta_1 \approx 0.940$, $\theta_2 \approx 0.057$.

4A. Experimental θ_j and densities of higher layer islands

Deposition of roughly 1 ML of Ag at 295 K with R≈0.055 ML/s yields (within ±0.005 ML) θ_1≈0.940 ML, θ_2≈0.057 ML, and θ_j=0 for j≥3, and a density of second layer islands of about 2.5×10^{-4}/site. See Fig. 7.

4B. Determination of the step-edge barrier

Since island formation is effectively irreversible at 295 K, we first analyze the observed multilayer growth by extending our model for irreversible submonolayer nucleation and growth of square islands to the multilayer growth regime, including a step-edge barrier and downward funneling [15]. After fixing E_d=325 meV, to precisely match the observed submonolayer island density with this model (see Sec. 3D), we adjust the only remaining free parameter, E_{Sch}, to match the observed layer coverages after deposition of 1 ML of Ag. The results shown in Table IV indicate that E_{Sch}≈25 meV. With this choice of E_{Sch}, the model also predicts a second layer island density of 4.3×10^{-4}/site at 1 ML, slightly higher but consistent with the experimental value, given the uncertainties in the latter. The estimate of E_{Sch} for Ag/Ag(100) homoepitaxy is substantially lower than that estimated for Fe/Fe(100) homoepitaxy [15,16], and that anticipated for Cu/Cu(100) homoepitaxy [15], but is certainly consistent with the "quasi-layer-by-layer" growth typically associated with Ag/Ag(100) at room temperature.

Table IV- Results for the layer coverage distribution at 295 K, from square island simulations with a fourfold-hollow geometry and deposition dynamics, using $E_{bond}=\infty$, $h/R\approx 5.1\times10^{7}$/s (i.e., E_d=325 meV, $\nu=10^{12}$/s, and the experimental $R\approx 0.055$ ML/s), and varying E_{Sch} between 15 and 35 meV. Coverages are in ML. The experimental layer coverages are $\theta_1\approx 0.940$ and $\theta_2\approx 0.057$ (± 0.005), which are matched by the simulations with $E_{sch}=25\pm5$ meV.

	E_{Sch}=15	20	25	30	35
θ_1	0.949	0.948	0.941	0.936	0.928
θ_2	0.048	0.049	0.056	0.061	0.069

4C. Predictions for multilayer kinetic roughening at 295 K

Having determined all parameters in our model, it is appropriate to examine its predictions for the subsequent multilayer kinetic roughening. Fig. 8 shows predictions for the film morphology after 1 ML, 50 ML, and 100 ML deposition of Ag, with R=0.055 ML/s. More generally, one monitors the evolution of the roughness, W defined as the standard deviation of the film height distribution. In terms of the fraction, $P_j=\theta_j-\theta_{j+1}$, of exposed atoms in layer $j\geq 0$, one has $W^2=\Sigma_{j\geq 0}(j-j_{av})^2P_j$, where $j_{av}=\theta=\Sigma_{j\geq 0}jP_j$, and $\Sigma_{j\geq 0}P_j=1$. Here W is in units of the interlayer spacing. Of primary interest is the exponent b, defined through the relationship $W\sim const\cdot\theta^b$, for large coverages or film heights, θ (i.e., after any initial oscillations in W have died out). At 295 K and $\theta\approx 20$ ML, we find $\beta=0.25\pm 0.05$, for $R\approx 0.055$ ML/s [30]. See Fig. 9. The Bragg intensity at the anti-phase condition, $I_{bragg}=(1-2\theta_1+2\theta_2-...)^2$ is plotted versus $\theta=\theta_1+\theta_2+...$ in Fig. 10. Consistent with experiment [5,6,21,22], the model predicts long-lived oscillations at 295 K.

4D. Discussion of uncertainties in the estimate of E_{Sch}

We now briefly discuss key sources of uncertainty in the estimate of E_{Sch}. Firstly, our modeling does not incorporate restructuring of growing islands upon coalescence to form larger squares (rather they continue growing as overlapping squares). Such restructuring inhibits downward transport, and if included in the model produces a substantially lower estimate for E_{Sch} [15]. Secondly, the value of 25 meV for E_{Sch} was obtained with the simplification that $E_{bond}=\infty$. Finally, we

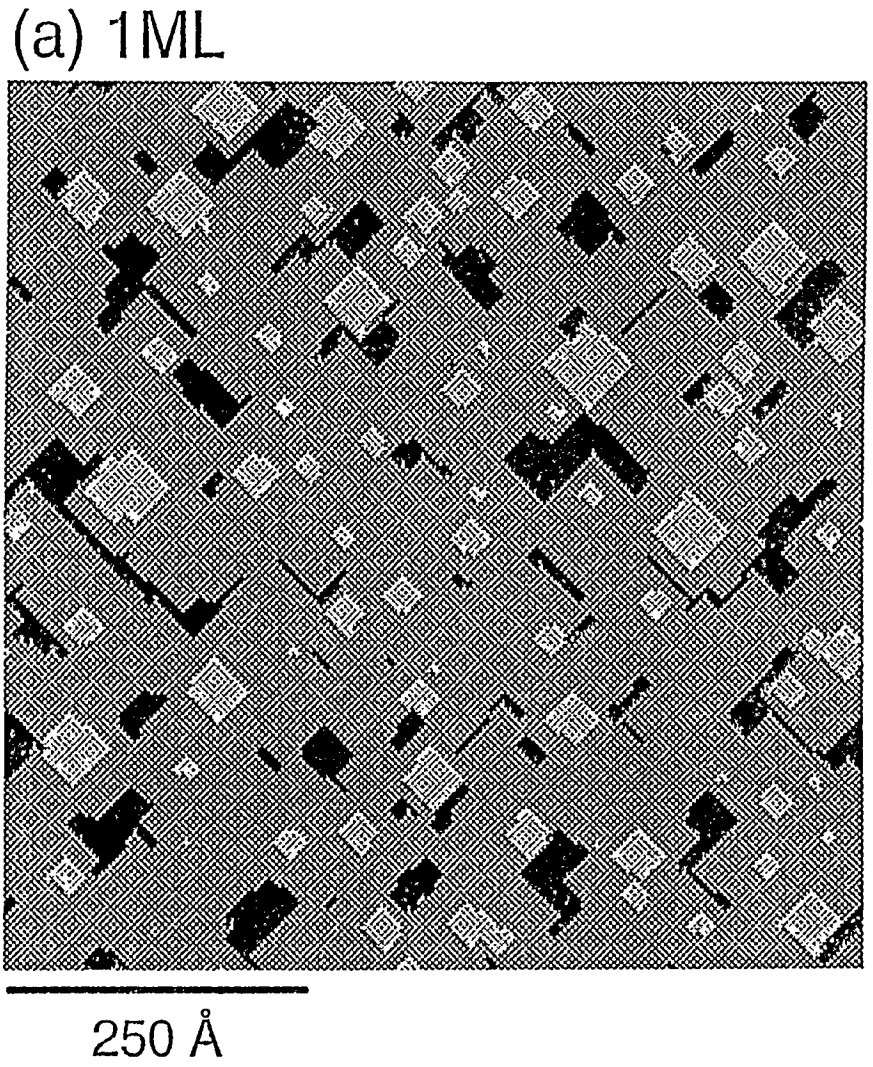

(a)

Figure 8. Snapshots of the surface obtained at (a) 1 ML, (b) 50 ML, and (c) 100 ML, from simulations with E_d=325 meV, E_{bond}=∞, and E_{sch}=25 meV, at 295 K for R=0.055 ML/s.

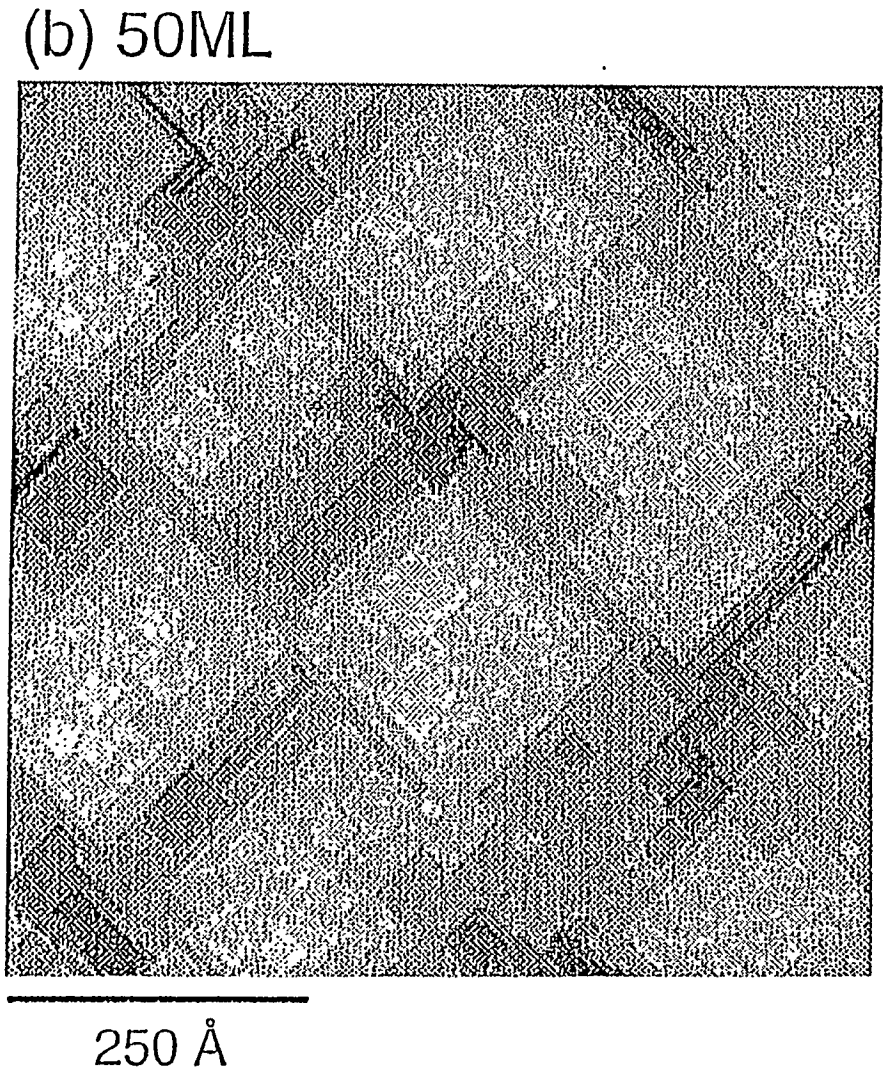

Fig. 8. (b)

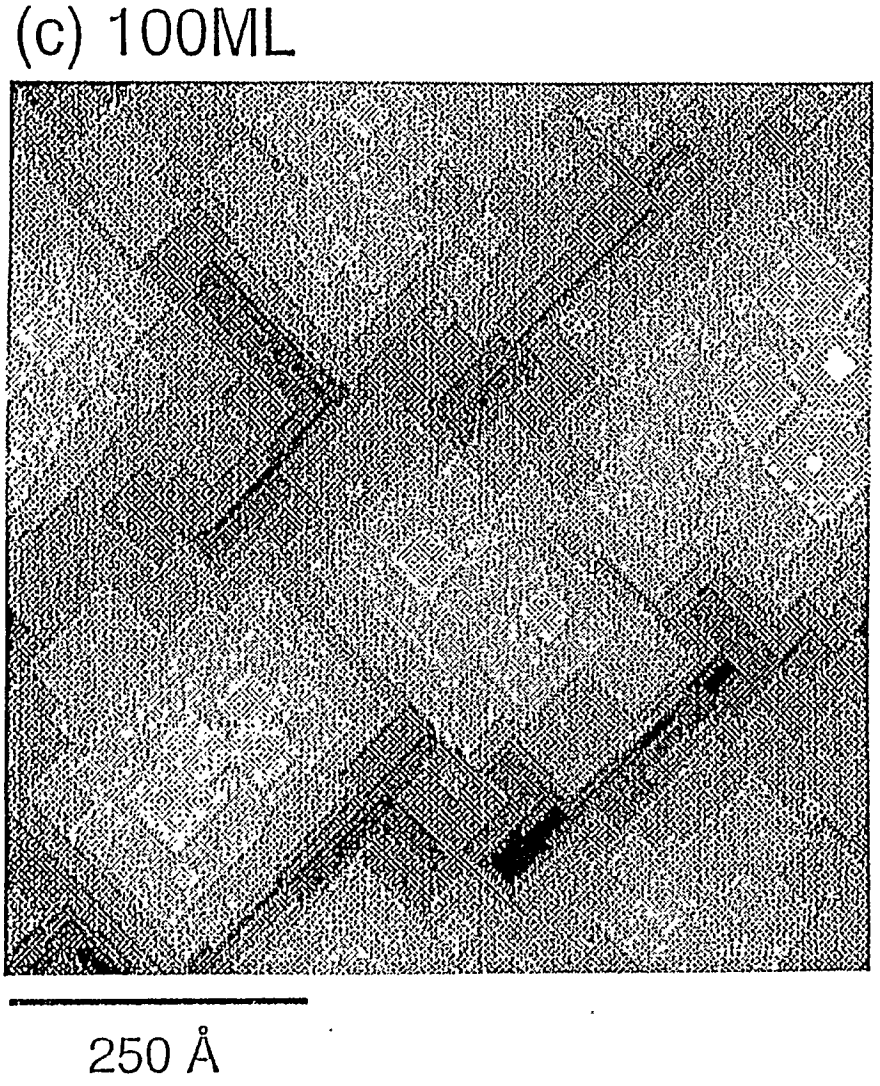

Fig. 8. (c)

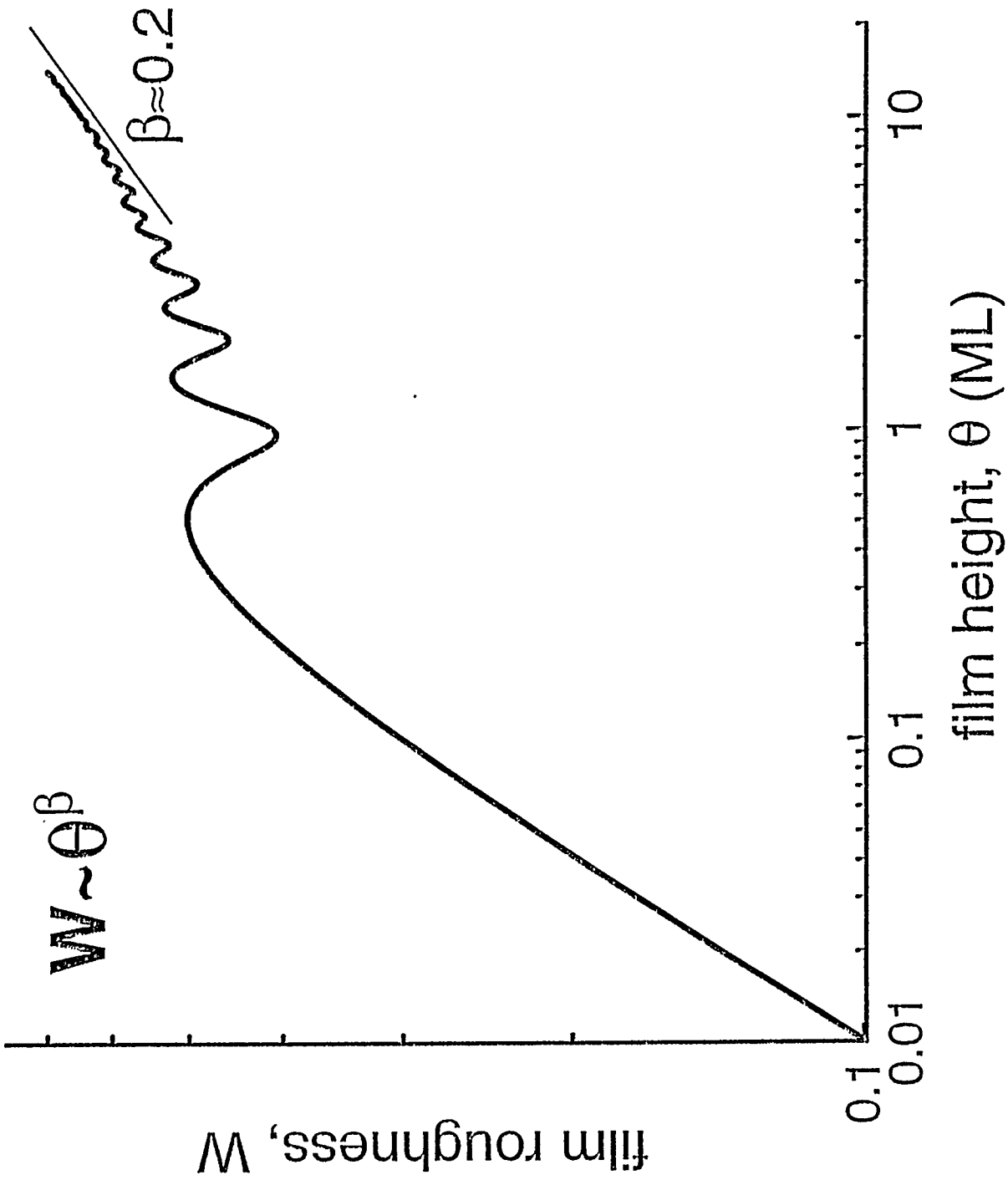
film roughness, W
film height, θ (ML)
0.01
0.1
1
10
0.1
W ~ θ^β
β≈0.2

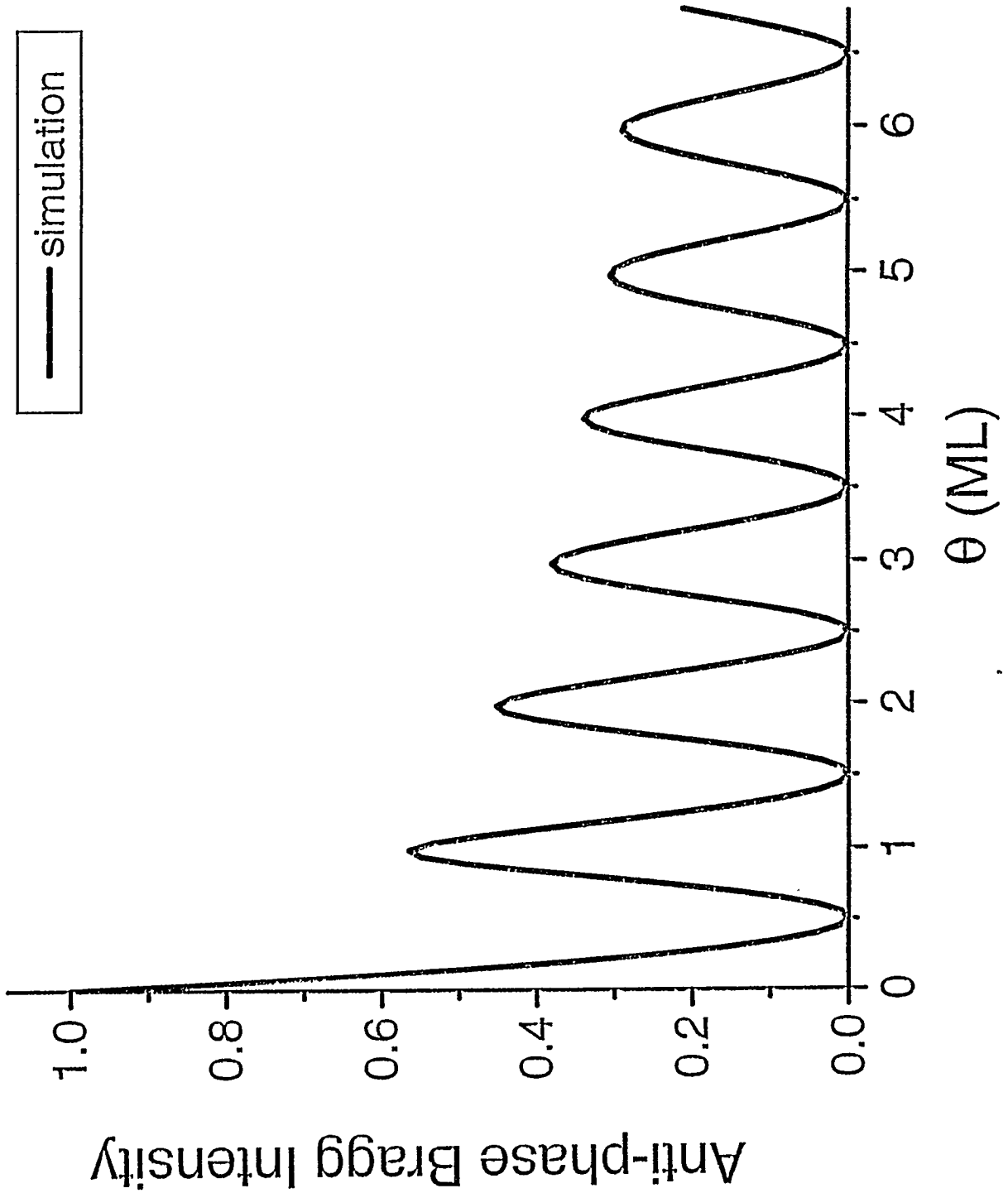
simulation
Anti-phase Bragg Intensity
1.0
0.8
0.6
0.4
0.2
0.0
0
1
2
3
4
5
6
Θ (ML)

note that a uniform step-edge barrier around the perimeter of the islands has been assumed. Certainly, a distinct barrier is possible at kink sites, so for this reason our estimate of E_{Sch} should be regarded as an effective barrier. Ref.[23] reports a Morse potential value of $E_{sch} \approx 370$ meV for straight (110) edges, which is far too high, but also notes distinct lower barriers for adatoms to descend at kink sites and at straight (100) edges (~140 meV).

4E. Temperature dependence of kinetic roughening

Our model can also be used to predict the temperature dependence of kinetic roughening [15]. As is generally the case for metal(100) homoepitaxy, we find that the roughness and the "effective" b vary significantly with T. In the range of 20 ML of Ag on Ag(100), with R=0.055 ML/s, we find that growth is smoother (i.e., with smaller W) above 295 K. Below 295 K, growth becomes progressively rougher down to about 200 K, below which re-entrant smooth growth is predicted by our model. Details will be discussed elsewhere.

5. Conclusions

By combining comprehensive STM studies with realistic modeling, we have obtained precise estimates of the key energies, $E_d \approx 330$ meV, $E_{bond} \approx 285$ meV, and $E_{Sch} \approx 25$ meV, controlling Ag/Ag(100) homoepitaxial growth.

References

[1] J.A. Stroscio, D.T. Pierce, and R.A. Dragoset, Phys. Rev. Lett. **70** (1993) 3615; J.A. Stroscio and D.T. Pierce, Phys. Rev. B **49** (1994) 8522; J.A. Stroscio, D.T. Pierce, M. Stiles, A. Zangwill, and L.M. Sander, Phys. Rev. Lett. **75** (1995) 4246.

[2] H.J. Ernst, F. Fabre, R. Folkerts, and H. Lapujoulade, Phys. Rev. Lett. **72** 1994) 112; H.J. Ernst, F. Fabre, and H. Lapujoulade, Phys. Rev. B **46** (1992) 1929; J.-K. Zuo, J.F. Wendelken, H. Dürr, and C.-L. Liu, Phys. Rev. Lett. **72** (1994) 3064; H. Dürr, J.F. Wendelken, and J.-K. Zuo, Surf. Sci. **328** (1995) L527.

[3] E. Kopatzki, S. Günther, W. Nichtl-Pecher, and R.J. Behm, Surf. Sci. **284** (1993) 154.

[4] D.K. Flynn-Sanders, J.W. Evans, and P.A. Thiel, Surf. Sci. **289** (1993) 75; **298** (1993) 378.

[5] Y. Suzuki, H. Kikuchi, and N. Koshizuka, Jap. J. Appl. Phys. **27** (1988) L1175.

[6] P. Bedrossian, B. Poelsema, G. Rosenfeld, L.C. Jorritsma, N.N. Lipkin, and G. Comsa, Surf. Sci. **334** (1995) 1.

[7] J.A. Venables, Philos. Mag. **27** (1973) 697.

[8] G. Ehrlich and H. Hudda, J. Chem. Phys. **44** (1966) 1039; S.C. Wang and G. Ehrlich, Phys. Rev. Lett. **70** (1993) 41; R.L. Schwoebel and E.J. Shipsey, J. Appl. Phys. **37** (1966) 3682; R.L. Schwoebel, J. Appl. Phys. **40** (1969) 614.

[9] J.W. Evans, D.E. Sanders, P.A. Thiel, and A.E DePristo, Phys. Rev. B **41** (1990) 5410; J.W. Evans, Phys. Rev. B **43** (1991) 3897; D.E. Sanders and J.W. Evans, in *The Structure of Surfaces III* (Springer, Berlin, 1991), p.38.

[10] C. Ratsch, P. Smilauer, A. Zangwill, and D.D. Vvedensky, Surf. Sci. **329** (1995) L599; C. Ratsch, A. Zangwill, P. Smilauer, and D.D. Vvedensky, Phys. Rev. Lett. **72** (1994) 3194.

[11] M.C. Bartelt, L.S. Perkins, and J.W. Evans, Surf. Sci. **344** (1995) L1193.

[12] J. Tersoff, A.W. Denier van der Gon, and R.M. Tromp, Phys. Rev. Lett. **72** (1994) 266.

[13] J.A. Meyer, J. Vrijmoeth, H.A. Van der Vegt, E. Vlieg, and R.J. Behm, Phys. Rev. B **51** (1995) 14790; P. Smilauer and S. Harris, *ibid*, **51** (1995) 14798.

[14] M.C. Bartelt and J.W. Evans, Surf. Sci. **298** (1993) 421; in *Common Themes and Mechanism of Epitaxial Growth*, ed. by P. Fuoss, J. Tsao, D.W. Kisker, A. Zangwill, and T. Kuech, Mater. Res. Soc. Symp. Proc. **312** (1993) 255.

[15] M.C. Bartelt and J.W. Evans, Phys. Rev. Lett. **75** (1995) 4250; in *Evolution of Epitaxial Structure and Morphology*, ed. by A. Zangwill, D. Jesson, D. Chambliss, and R. Clarke, Mater. Res. Soc. Symp. Proc. **399** (1996) 89; J.W. Evans and M.C. Bartelt, Langmuir **12** (1996) 217.

[16] J.G. Amar and F. Family, Phys. Rev. B **52** (1995) 13801.

[17] P. Smilauer and D.D. Vvedensky, Phys. Rev. B **52** (1995) 14263.

[18] Non-trivial "capture areas" can be identified via Molecular Dynamics simulations for each fourfold-hollow (FFH) adsorption site configuration. In the Monte Carlo simulations we use a discrete version of these: two sub-lattices define on-top and FFH sites, and atoms impinging on the former deflect down until they reach a FFH site. Modifications which allow for larger fractions of

atoms impinging on on-top sites to stay on the top layer may affect predictions for the late-stage roughening behavior.

[19] Ch. Ammer, Solid State Phenom. **12** (1990) 73; Ch. Teichert, Ph.D. thesis (unpublished, Universitaat Halle, 1992).

[20] W.F. Egelhoff and I. Jacob, Phys. Rev. Lett. **62** (1989) 921.

[21] H.A. van der Vegt, W.J. Huisman, P.B. Howes, and E. Vlieg, Surf. Sci. **330** (1995) 101.

[22] W.C. Elliott, P.F. Miceli, T. Tse, and P.W. Stephens, Physica B, in press (1996); presentation at the Fall MRS Meeting (Boston, 1995), and preprint.

[23] Ch. Teichert, Ch. Ammer, and M. Klaua, Phys. Stat. Sol **A146** (1994) 223.

[24] J.-M. Wen, J.W. Evans, M.C. Bartelt, J.W. Burnett, and P.A. Thiel, Phys. Rev. Lett. **76** (1996) 652; J.-M. Wen, S.-L. Chang, J.W. Burnett, J.W. Evans, and P.A. Thiel, Phys. Rev. Lett **73** (1994) 2591.

[25] This result was obtained from the fluctuation-correlation relation connecting fluctuations in island number with correlations in their spatial locations, and incorporating information on the island separation distribution for i=1 [J.W. Evans and M.C. Bartelt, Surf. Sci. **284** (1993) L437].

[26] We do not incorporate stable cluster mobility in our model, as we have no clear evidence supporting its significance here (on the time scale of deposition). If it was significant, then the observed χ would have to be at least ~0.4 (for i=1). See J. Villain, A. Pimpinelli, L. Tang, and D. Wolf, J. Phys. (France) **I 2** (1992) 2107; J. Villain, A. Pimpinelli, and D. Wolf, Comments Condens. Matter Phys. **16**

(1992) 1; M.C. Bartelt, S. GÅnther, E. Kopatzki, R.J. Behm, and J.W. Evans, Phys. Rev. B **53** (1996) 4099.

[27] M.C. Bartelt and J.W. Evans, Phys. Rev. B **46** (1992) 12675; M.C. Bartelt, M.C. Tringides, and J.W. Evans, in *Evolution of Surface and Thin Film Microstructure*, ed. by H.A. Atwater, E. Chason, M.H. Grabow, and M.G. Lagally, Mater. Res. Soc. Symp. Proc. **280** (1993) 363.

[28] J.W. Evans and M.C. Bartelt, J. Vac. Sci. Technol. A **12** (1994) 1800; J.G. Amar and F. Family, Phys. Rev. Lett. **74** (1995) 2066.

[29] However, if $E_{bond}/E_d<<1$ (so all islands can dissociate) or $E_{bond}/E_d>>1$ (so island formation is irreversible), then N_{av} depends only on E_d.

[30] If we choose $R\approx0.2$ ML/s to match the flux in surface X-ray scattering investigations of the kinetic roughening of Ag/Ag(100) [22], our model predicts that $\beta\approx0.2$ at 300 K, for θ=10-20 ML, consistent with the experimental estimate of $\beta=0.17\pm0.02$ in the same coverage range. At 200 K, we find $\beta\approx0.27$ and the experiment gives $\beta=0.28\pm0.03$. However, for both T, the actual values of W from the simulations are 20-30% smaller than the values reported from experiment.

[31] J. Villain, J. Phys. I (France) **1** (1991) 19; M. Siegert and M. Plischke, Phys. Rev. Lett. **68** (1992) 2035; *ibid* **73** (1994) 1517; Phys. Rev. E **50** (1994) 917; *ibid* **53** (1996) 307; J. Krug, M. Plischke, and M. Siegert, Phys. Rev. Lett. **70** (1993) 327; M.D. Johnson *et al.*, *ibid* **72** (1994) 116; C.J. Lanczycki and S. DasSarma, *ibid* **76** (1996) 780.

Appendix A - Transitions in i for metal(100) homoepitaxy

Here we develop precise criteria to analyze transitions in critical size, i, for unreconstructed metal(100) homoepitaxy, based on the behavior of the average island density, with temperature (T) and flux (R), from simulations of nucleation and growth of square-islands. We also compare with results from simple rate equations [11]. These criteria can be used to estimate transition temperatures given the terrace diffusion barrier, E_d, and adatom-adatom bond energy, E_{bond}, or vice- versa.

We focus on the "low" temperature regime, where i is small, and assume throughout that the binding energy of a critical cluster (of i atoms) is approximately given by the number of nearest-neighbor adatom bonds in the cluster times E_{bond}. In this case, one expects in these systems a transition with increasing T (at fixed F) or decreasing F (at fixed T) from i=1 (where single bonds are stable) directly to i=3 (where double bonds are stable), without a significant regime of i=2 behavior. Doubly-bonded adatoms dissociate at substantially higher T. The i=3 regime is better defined (extending over larger T or F ranges), the larger the ratio E_{bond}/E_d [11]. It is an "unconventional" i=3 regime, in that tetramers, hexamers, etc. are stable, but not pentamers, septamers, and other configurations with singly-bonded atoms.

Certainly, crossover behavior should be determined by the relative magnitudes of the dissociation rates of dimers or trimers and the rate at which adatoms aggregate (thereby stabilizing) dimers or trimers. As shown in Ref.[11], this leads to a natural "crossover variable", $Y=\exp[-3E_{bond}/(2k_BT)](h/R)$, which

increases monotonically across the transition from i=1 to i=3. In terms of Y, the criteria marking the end of the i=1 regime, and beginning of i=3 scaling (and eventual demise of i=3 behavior) are basically independent of system parameters [11].

Next we examine this transition by monitoring the effective value of the flux-exponent, $\chi = d(ln\ N_{av})/d(ln\ F)$, for increasing T, at fixed coverage, θ. The data for N_{av} were obtained from simulations of square-islands [14], where we allow dissociation of single and double bonds, with rates $\exp[-E_{bond}/(k_BT)]h$ and $\exp[-2E_{bond}/(k_BT)]h$, respectively. Fig. A shows the results for χ versus Y. From the simulation data, we identify the upper-T limit, T_{1+}, of the i=1 regime as given by $Y_{1+}=Y(T=T_{1+})\approx 3$, the lower-T limit, T_{3-}, of the "i=3" regime by $Y_{3-}=Y(T=T_{3-})\approx 10^3$, and the upper-T limit, T_{3+}, of the "i=3" regime by $Y_{3+}=Y(T=T_{3+})\approx 3\times 10^3$. Fig.A shows also results for χ versus Y from simple rate-equations [11]. The most dramatic differences relative to the simulation results are the shifts (to smaller values) in the rate-equation predictions for the transition temperatures [11], implying that the transitions in χ are delayed in the simulations relative to the rate-equations. This is a direct consequence of the neglect of dissociation-recondensation events (from and to the same island) in the rate equations. These events, associated with the space-filling property of two-dimensional random walks, clearly provide additional pathways for island stabilization, which are not accounted for in the rate equations. Thus, for fixed E_d, the rate equations overestimate E_{bond}.

For Ag/Ag(100) homoepitaxy, where we estimate $E_d \approx 330$ meV and $E_{bond} \approx 285$ meV, for a typical $\nu \approx 10^{12}$/s, we find $Y(T=295K) \leq Y_{1+}$, for R≈0.1-0.01ML/s, but Y(295 K) in the transition region from i=1 to i=3, for R≈0.001 ML/s or smaller.

Figure A. Transition in χ with increasing Y. Symbols are from simulations where we used ν=1012/s, R=0.06 ML/s, and θ=0.1 ML, with E_d=325 meV, E_{bond}=325 meV (•). The solid line is from rate equations [11], using the same parameters. Dashed lines are asymptotic limits for i=1 (1/3) and i=3 (3/5).

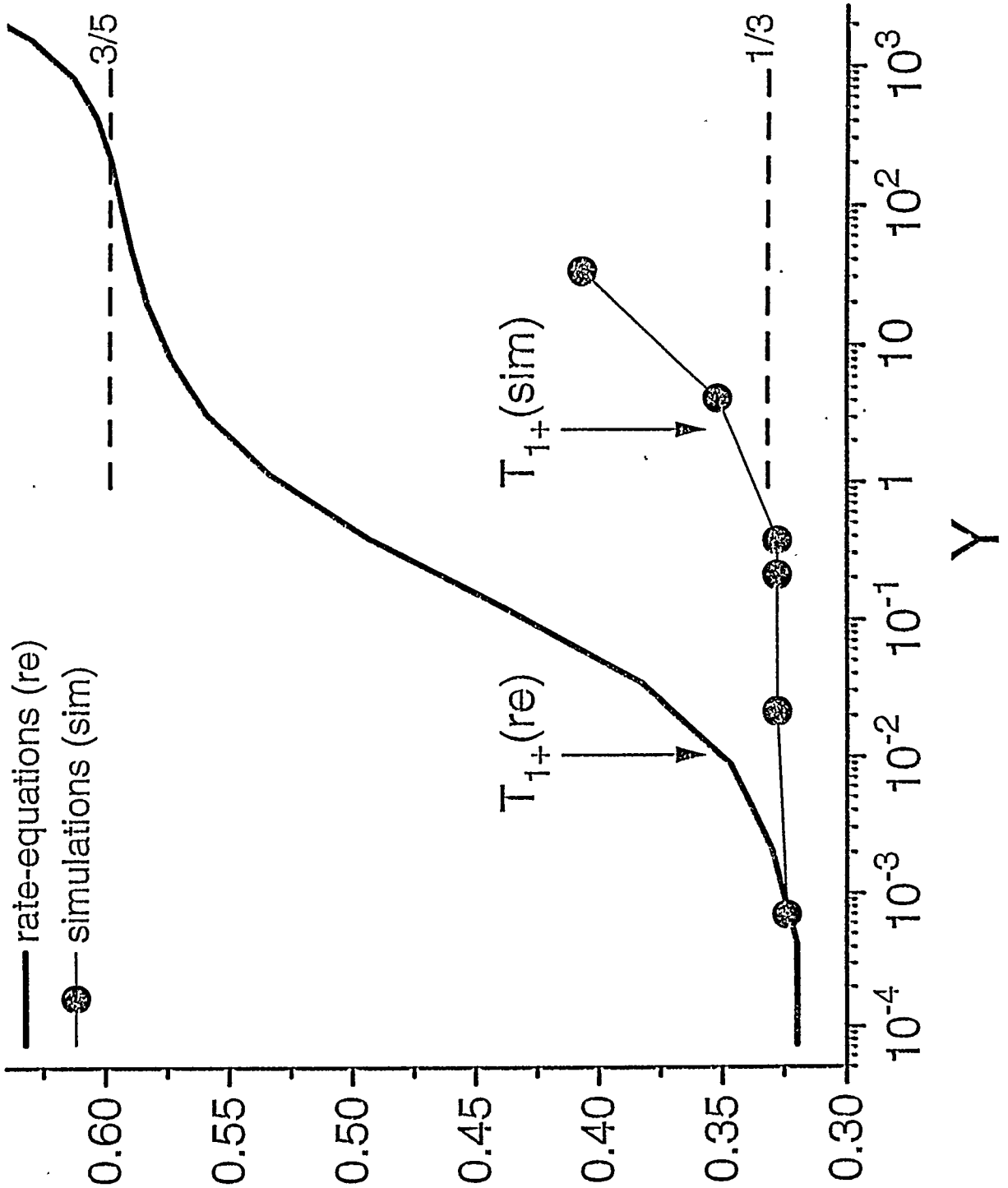
rate-equations (re)
simulations (sim)
3/5
1/3
T_{1+}(sim)
T_{1+}(re)
χ
Y
0.60
0.55
0.50
0.45
0.40
0.35
0.30
10^{-4}
10^{-3}
10^{-2}
10^{-1}
1
10
10^{2}
10^{3}

CHAPTER 3

GENERAL CONCLUSION

Thin film growth is very important in many respects. During film growth, adatoms have a certain lifetime to undergo different processes after being deposited onto a substrate. In homoepitaxial growth, film growth will not follow theoretically predicted layer-by-layer growth due to kinetic limitations ("kinetic roughening"). Atomic-scale processes, such as diffusion on terraces, diffusion over terraces, and coalescence into growing islands, can be described by individual energy barriers. Bond energy (E_{bond}) can describe the major interaction between adatoms; diffusion energy (E_d) can describe the migration of adatoms on the substrate; and step edge barrier (E_{sch}) can describe the diffusion of adatoms through terraces.

It was the purpose of this work to determine these energy values. By combining comprehensive STM studies with realistic modeling, we were able to obtain precise estimates of above mentioned energies: $E_d \approx 330$ meV, $E_{bond} \approx 285$ meV, and $E_{sch} \approx 25$ meV, for Ag/Ag(100). A prediction of multilayer roughness of Ag/Ag(100) films based on the energy values we obtained was also presented.

Additional work could be done to check the correctness of the model we established, such as multilayer growth. Temperature dependent experiments could be done in a more sophisticated way if given appropriate instruments. Finally, similar measurements for different orientations of Ag substrate are useful to compare these energy values governing the kinetic roughening.

ACKNOWLEDGMENTS

First of all, I would like to express my gratitude to my research advisor, Professor Patricia A. Thiel, for her patience, support, and understanding during my time as a graduate student in the Department of Chemistry at Iowa State University.

I thank all members of the Thiel group. I am greatly indebted to Dr. Jianming Wen for his generous help in my starting stages of operating STM. I appreciate the help from Dr. Cynthia Jenks, especially in the STM image processing.

I thank Professor James Evans and Dr. M.C. Bartelt for their great contribution to this work and their helping with my thesis.

Finally, I am thankful to my wife for her support and love.

This work was performed at Ames Laboratory under contract No. W-7405-Eng-82 with the U.S. Department of Energy. The United States government has assigned the DOE Report number IS-T 1783 to this thesis.

APPENDIX I

OXYGEN ADSORPTION ON A SINGLE-GRAIN, QUASICRYSTAL SURFACE

A paper published in the Surface Science

S.-L. Chang, W. B. Chin, C.-M. Zhang, C. J. Jenks, and P. A. Thiel

ABSTRACT

Oxygen adsorbs on the five-fold surface of $Al_{70}Pd_{21}Mn_9$. A chemisorbed phase, possibly in or below the surface plane, serves as a precursor to oxidation of Al. This chemisorbed phase destroys the quasiperiodicity of the surface. The major features of oxygen adsorption and oxidation are similar in the temperature range 105-500 K, but are different at 870 K, where Al segregates strongly to the surface. We postulate that Al segregation is driven by the exothermicity of its oxide, which is higher than that of the other constituents of this alloy. At all temperatures, the oxide layer is passivating (under the conditions of these experiments), is quite thin (< 10Å), is thermally stable (at least upon heating to 870 K), and may differ chemically from bulk Al_2O_3. The oxidation characteristics of this quasicrystal are broadly similar to those of its major constituent, Al, with the possible exception of the oxygen sticking coefficient.

1. Introduction

Quasicrystals are materials which contain a symmetry element, such as a five-fold axis, which is crystallographically forbidden, and which has long-range,

aperiodic order [1-7]. This symmetry is typically revealed by bulk diffraction techniques, although it can be manifest also in other ways, such as the macroscopic particle shape. Several models have been proposed to explain the bulk structure of quasicrystals, notably the Penrose tiling, glass, and entropy models.[3] In all models, the quasicrystal is composed of a group of subunits arranged in such a way as to yield the apparently-forbidden periodicity.

Previous studies of the surface properties of quasicrystalline materials are scarce.[8-15] It appears that there are two reasons for this scarcity. First, it has been difficult to obtain single-grain samples which are large enough for the typical probes of surface science, such as Auger electron spectroscopy (AES) or low-energy electron diffraction (LEED). These probes typically require a sample no less than about 2 mm x 2 mm in area. However, special techniques may be used successfully to prepare boules of some quasicrystals containing single grains large enough for surface probes,[16] and we are fortunate to have suitable samples available to us. (See Section 2.) Second, it has been thought that these materials are intriguing from the point of view of fundamental physics and chemistry, but have very limited (or no) practical use. Recent work has shown, however, that coatings prepared from quasicrystalline materials may be quite useful. For instance, DuBois and coworkers showed that such coatings can have such a low coefficient of friction that they rival Teflon in some applications, notably in non-stick cookware.[17-22] Also, the coatings can be highly resistant to wear[23] and corrosion.[19, 22] This resistance, plus the fact that the quasicrystalline films can be prepared in an environmentally-benign manner,

may make them attractive as alternatives to chemically-based platings of machine parts.

It is our purpose to investigate the oxidation behavior of the quasicrystals, in the hope of determining factors which may contribute to their corrosion resistance. Oxygen or oxide layers are also of interest because of their possible role in determining the tribological properties of these materials.[23] Of the other published literature dealing with quasicrystal surfaces, none deals with chemisorption, much less oxidation, as does our study.

For this work, we choose $Al_{70}Pd_{21}Mn_9$ (where composition is given in atomic %) because we can obtain it in single grains large enough to accommodate our probes. The thermodynamically-stable phase of this material, up to the melting point (1123 K), is icosahedral, i.e. it possesses an apparent five-fold axis.[24] It is metallic, but with very low electrical conductivity.[25, 26]

2. Experimental description

Most experiments are performed in a stainless-steel ultrahigh-vacuum chamber (base pressure $< 1 \times 10^{-10}$ Torr) equipped with a single-pass cylindrical mirror analyzer for AES; quadrupole mass spectrometer; μ-metal-shielded, display-type, four-grid LEED optics; sputter gun; and provisions for gas exposure. The Auger beam current density is measured at $1.5\mu A/mm^2$; this must, however, be taken as a lower limit since the sample is not biassed to retard secondary emission during measurement. The Auger beam energy is 3 keV. Some x-ray photoelectron (XPS) measurements are also made on a Perkin Elmer

instrument, Model 5500, equipped with ACCESS software. More details are given elsewhere.[27]

The quasicrystal boule, consisting of several single grains, is grown by Dr. T. Lograsso and D. Delaney at the Materials Processing Center of Ames Laboratory, using the Bridgman method.[16, 28] The composition of the starting material is 70-21.5-8.5 (Al-Pd-Mn), and chemical analysis of parts of ingots grown in this way indicate a composition of 70.5-20.5-9; hence, we will quote a nominal composition for our bulk sample of 70-21-9. The sample, a flat pentagonal wafer approximately 5mm x 3mm x 1.5mm in size, is cut from a single grain with a five-fold axis normal ($\pm 0.3^{o}$) to the surface. It is mechanically polished to a mirror finish with 1 μ diamond paste, and then electropolished. A different, but very similar, sample is used for the XPS measurements.[27]

The sample cannot be spotwelded because it is a poor electrical conductor, and it shatters when spotwelding is attempted. Thus, for experiments in vacuum, the sample is placed between two thin Ta plates (15 mm x 15 mm) spot-welded together. A hole of about 3 mm diameter in the front plate exposes the sample surface for ion sputtering, LEED and AES. (Care is taken to use an ion beam which is small enough to sputter only the quasicrystal--hence avoiding contamination of the surface with Ta--but large enough to clean the quasicrystal uniformly.) One thermocouple (W/5%Re vs W/26%Re) is spot-welded on the back tantalum plate for real-time control of crystal temperature. A second is wedged between the crystal and the front plate to allow occasional checks of thermal homogeneity. The sample-plate assembly is mounted on a manipulator

with high-current feedthroughs for resistively heating the Ta plates, and a liquid-nitrogen cold finger for cooling. The sample is heated by thermal conduction from the Ta plates. The maximum temperature we use in working with this sample, under any circumstance, is 870 K (250 K below the melting point).

After exposure to atmosphere, the sample surface is cleaned in vacuum by repeated cycles of ion bombardment (Ar^+, 1.0 keV) at room temperature for 1 hour and annealing at 870 K for four hours, until oxygen or other impurities are reduced to the noise level of AES. This treatment produces a sharp five-fold LEED pattern. Oxygen exposures are carried out by backfilling the chamber with pressures of 2×10^{-8} Torr for low exposures, or 5×10^{-7} Torr for high exposures. After exposure to oxygen in vacuum, the sample is cleaned with the same ion bombardment-annealing cycles, to the extent necessary.

Intensity-energy, or I(E), curves for the diffraction spots are acquired at normal incidence with a computer-interfaced video processor and a silicon-intensified-target camera.[29] Background subtraction is performed locally around each spot during data collection. LEED I(E) measurementsare performed with the sample at 105 K.

3. Experimental results

3A. Characterization of the clean surface

Chemical composition. Figure 1a shows an Auger spectrum of the clean alloy surface, after extensive cleaning and annealing in vacuum. The peaks assigned to Pd, Mn, and Al are so labelled. Assuming that composition is

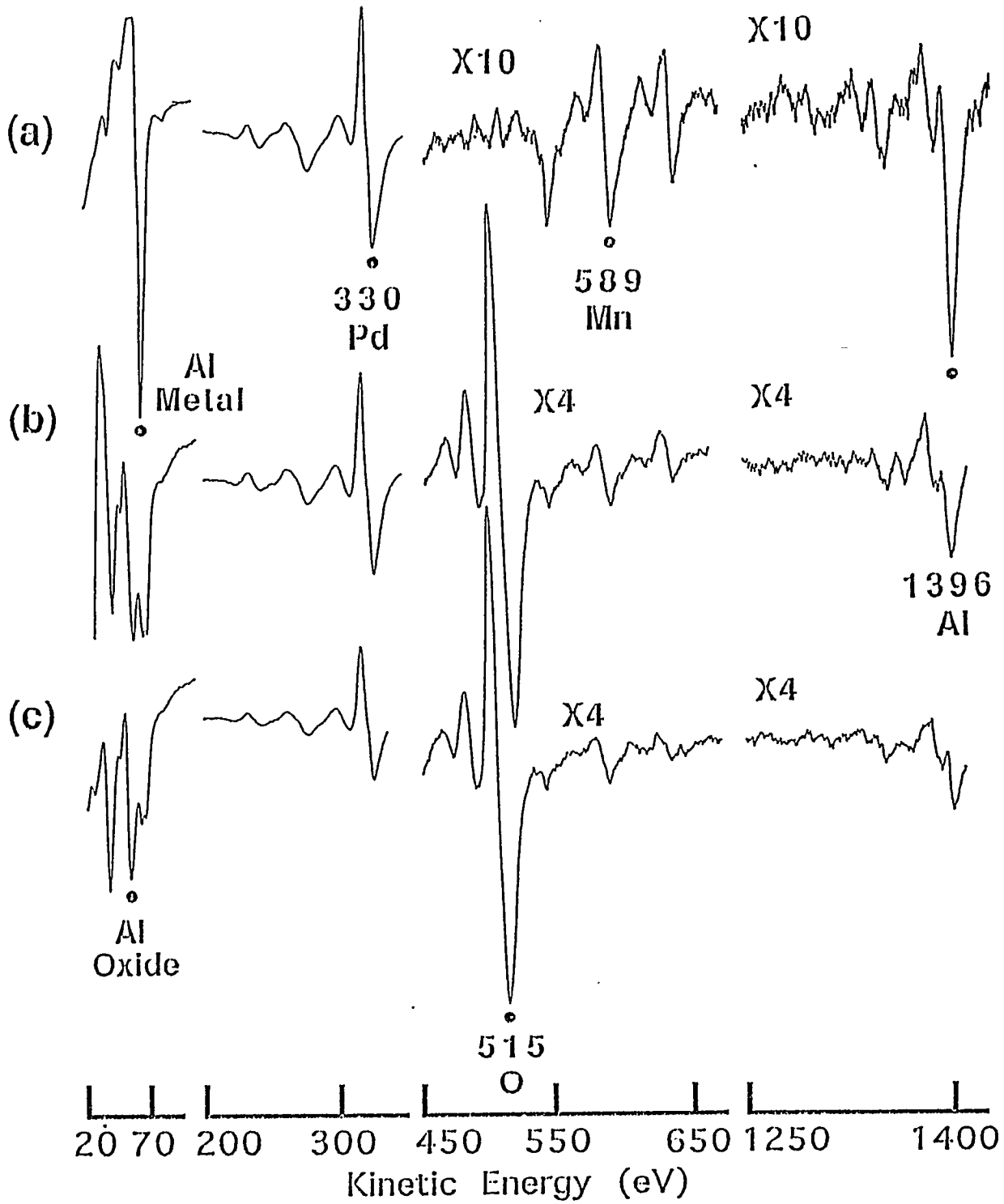
(a)
(b)
(c)
X10
X10
330
Pd
589
Mn
Al
Metal
X4
X4
1396
Al
X4
X4
Al
Oxide
515
O
20 70 200 300 450 550 650 1250 1400
Kinetic Energy (eV)

uniform up to the surface plane, a standard approach can be implemented to derive chemical composition from AES data.[30] The surface composition so derived is $Al_{67\pm2}Pd_{26\pm2}Mn_{7\pm1}$, where the error bars represent a statistical confidence limit of 99% based on repetitive sampling, i.e. they indicate precision, not accuracy. The surface composition derived from XPS, for a sample treated similarly, is $Al_{71}Pd_{23}Mn_{6}$. These surface compositions measured via AES and XPS, 67-26-7 and 71-23-6, respectively, are fairly close to the bulk composition of 70-21-9. {The differences between data from the AES and XPS techniques, for instance, probably reflects the level of accuracy inherent in this type of compositional analysis.}

Because accuracy is far more difficult to assess than precision, the *values* of surface composition quoted above are not so significant as *changes* in the composition which may occur, for instance, upon heating or upon sputtering. We find by AES that the composition of the clean surface is constant between 105 and 500 K. While AES alone indicates a slight, reversible change at 870 K to $Al_{73\pm6}Pd_{19\pm4}Mn_{8\pm2}$, i.e. 73-19-8, XPS does not support this and so we believe the AES intensities are influenced more by lineshape changes than compositional changes at elevated temperatures.[27] Immediately after ion bombardment, without annealing, the surface is highly enriched in Pd. The measured composition is $Al_{48\pm2}Pd_{45\pm2}Mn_{7\pm1}$, i.e. 48-45-7. This probably results from a preferential sputtering effect, i.e. preferential removal of the Al during ion bombardment.

The compositions of the clean surface, and of the surfaces which form upon oxidation, are listed in Table 1.

LEED pattern. The surface normal of our sample is denoted [0,0,0,0,0,1], using the full six-dimensional nomenclature appropriate for the bulk crystal. This means that the surface plane is perpendicular to the five-fold axis. The LEED spots are indexed using five basic vectors, i.e. using the two-dimensional projection of the bulk basis vectors which is appropriate for a grain with this orientation.[9] The five-fold periodicity of the surface is evident in the LEED photograph of Fig. 2a, and also in the schematic representation of Fig. 2b.

In the LEED pattern, up to three sets of bright diffraction spots are visible in the energy range 70 to 260 eV. (In Fig. 2a, the incident energy is such that only the first two sets are visible.) Each set is comprised of ten spots equidistant from the origin, i.e. on a ring. Hence, we refer to these sets as the first, second, and third ring. (An additional ring, even smaller than the first, can be viewed very close to the origin, but its spots are quite weak and are normally blocked by the sample holder.) The ratios of the radii of the concentric rings are, within error, equal to those predicted by the Golden Mean.[31, 32] Each ring contains two sets of non-equivalent spots arranged in a pentagon. In addition, there are many weaker diffraction spots, such as those represented by open circles in Fig. 2b.

The diffraction pattern of the clean surface is visible in the temperature range 105-500 K, but is not detectable at 870 K. This could be due to Debye-Waller attenuation, or distortion in the pattern from magnetic fields induced by heating. In either case, the highest temperature is not accessible for LEED studies.

Table 1. Elemental compositions of bulk and surface regions of the quasicrystal, after various treatments. Accuracies are difficult to assess, but are probably about ± 10% with either AES or XPS. The data should be used more heavily to determine *changes* fter various treatments, when surface composition is measured with the same technique. To this end, statistical uncertainties (based upon multiple measurements) are given as 99% confidence limits for AES data, and 67% confidence limits for XPS data. AES and XPS data are obtained on two different samples.[27]

Sample and treatment	Composition (atomic %)			Technique
	Al	Pd	Mn	
Nominal bulk composition	70	21	9	see Sec. 2
Clean, annealed surface, measured at T ≤ 500 K.	70.5±0.8 67±2	23.1±0.6 26±2	6.4±1.2 7±1	XPS [27] AES
Freshly sputtered surface, sputtered and measured at 300 K.	48±2	45±2	7±1	AES
Surface after 104 L O2 exposure, oxidized and measured at 500 K.	73±1	21±1	6±1	AES
Surface after 104 L O2 exposure, oxidized and measured at 870 K.	89±1 78.9 ± 0.8	7±1 17.3 ± 0.1	4±1 3.8 ± 0.8	AES XPS [27]

Figure 2. LEED patterns for the quasicrystal surface. (a) Photograph of the clean surface at V_e = 85 eV, normal incidence, T = 105 K. (b) Schematic representation of photograph in (a), defining the spot indices and the "rings." The first ring is indicated by the smallest arc and its spots are shown as circular symbols. The second ring is indicated by the largest arc and its spots are shown as squares. Within each ring, there are two sets of inequivalent beams which are indicated by filled and shaded symbols, respectively. These two sets are defined by the tips of two pentagons which are rotated by 90^o. Open circles are satellite spots. Starting at the top right on the first ring and moving clockwise, the 7 spots shown are the (00100), (0000-1), (01000), (000-10), (10000), (00-100), and (00001). Starting at top right on the second ring and moving clockwise, the 7 spots visible are named (-1000-1), (01100), (000-1-1), (11000), (00-1-10), (10001), and (0-1-100). The third ring is not shown, but its spots are named similarly. (c) Photograph of the surface as in (a), but after 5 L O_2 at 105 K. (d) Photograph as in (a), but after 10 L O_2 at 105 K.

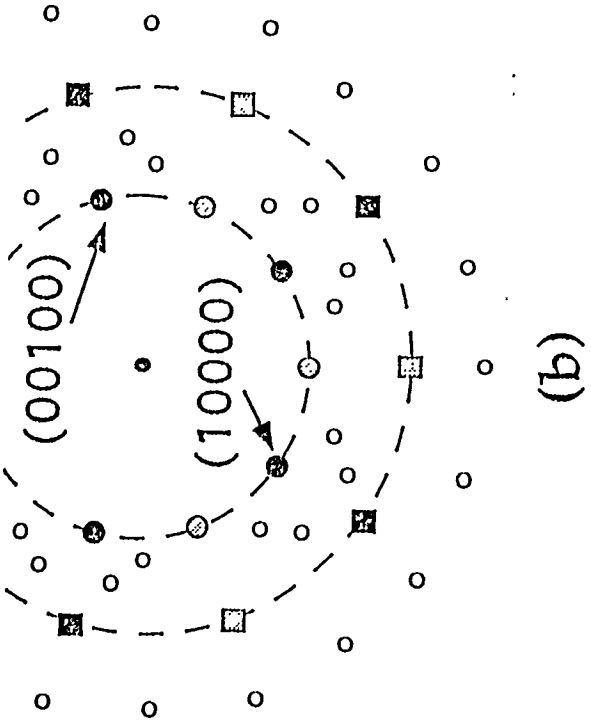

(b)

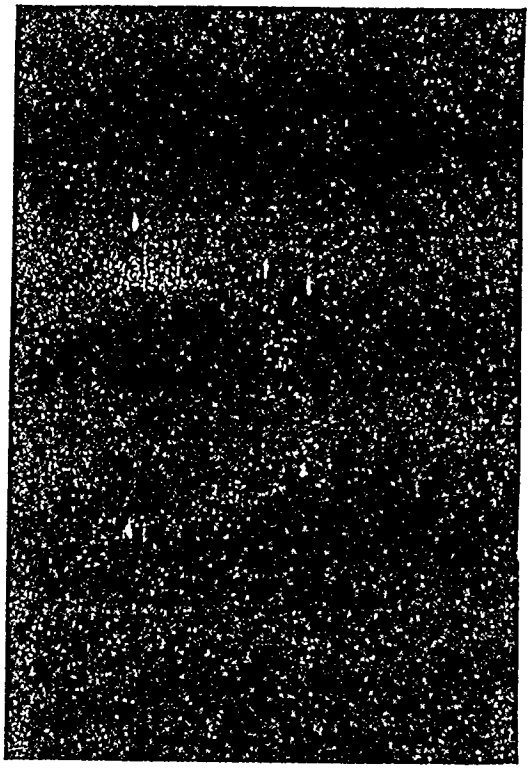

(d)

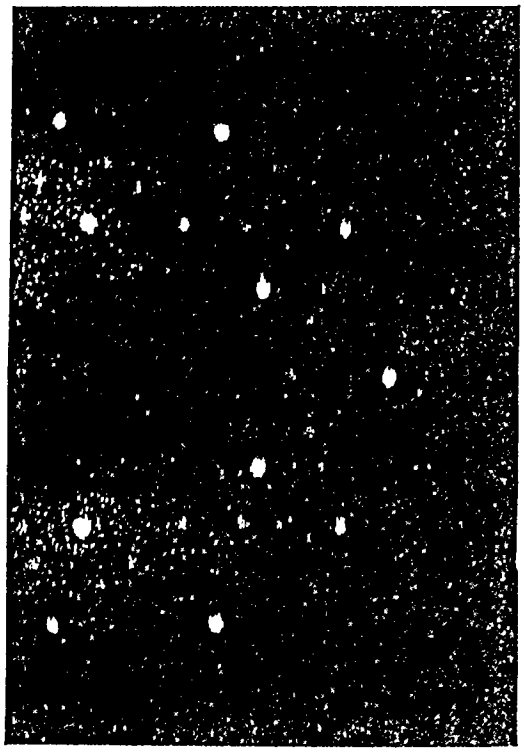

(a)

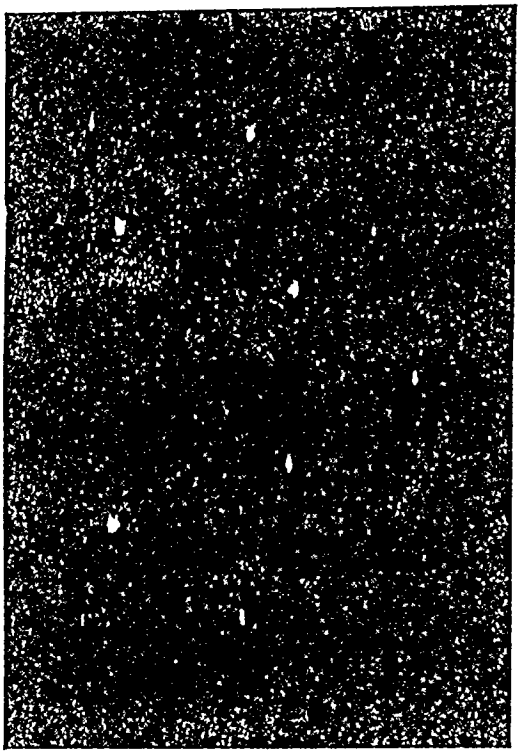

(c)

3B. Exposure to oxygen.

AES. The AES data of Figure 1b and 1c show that exposure to oxygen does cause adsorption of oxygen, signalled by the emergence of the characteristic oxygen transition at 515 eV. In Fig. 3, the absolute intensity of this transition is given as a function of exposure, for four different sample temperatures: 105, 300, 500, 870 K. At the three lower temperatures, the signal increases monotonically, reaching saturation by ca. 50 L exposure. At the highest temperature, the oxygen signal rises more slowly, reaching saturation only by ca. 160 L. The saturation values change only slightly when exposure is increased from 200 to 11,000 L, as shown. Whether measured at 200 or 11,000 L, the saturation value decreases significantly as surface temperature increases from 120 to 870 K, an effect which we do not understand at this time. Within experimental error, the initial sticking coefficient (which is proportional to the slope of the curves of Fig. 3 near zero exposure) does not depend upon temperature. We check these curves for artifacts due to electron beam damage by changing the exposure-interval of the measurement, and find no evidence for such effects.

One concludes from Fig. 3 that there is no strong temperature-dependence in the oxygen adsorption kinetics, between 105 and 500 K. However, oxygen adsorption proceeds differently at the highest temperature studied, 870 K. This trend will be obvious also in other data.

Exposure to oxygen also attenuates the characteristic metal transitions, as shown in Fig. 1. A first question is whether these intensities decline in parallel, or whether there is a change in the surface composition upon oxygen adsorption.

Figure 3. Intensity of the oxygen Auger transition at 515 eV as a function of oxygen exposure.

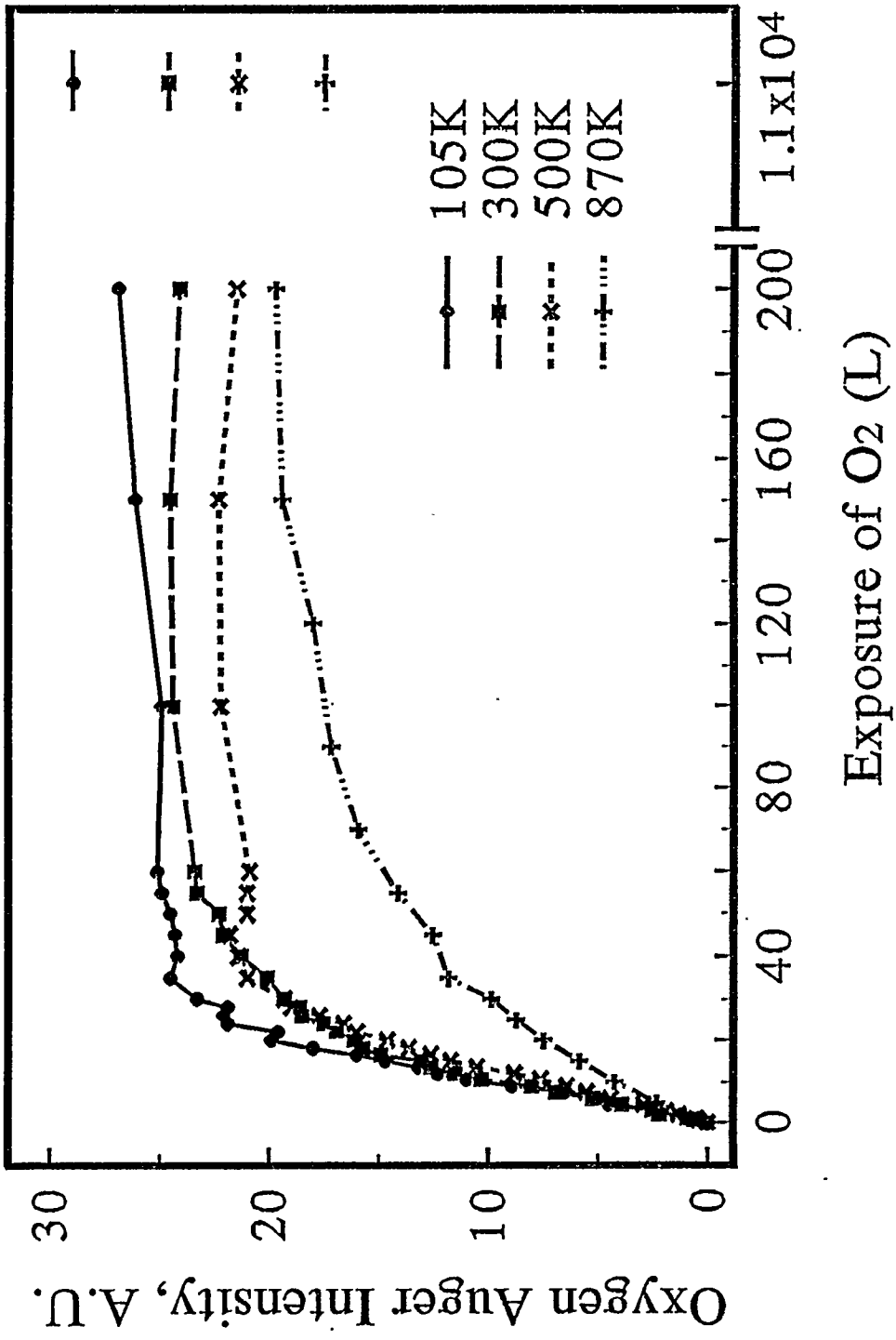
Oxygen Auger Intensity, A.U.
0
10
20
30
0
40
80
120
160
200
1.1x104
Exposure of O2 (L)
105K
300K
500K
870K

To answer this, the three high-energy transitions (1396 eV-Al, 330 eV-Pd, and 589 eV-Mn) are used. Figure 4a shows the absolute intensities of the metal transitions, while Fig. 4b shows the metal compositions derived from those intensities, as functions of oxygen exposure at 500 and 870 K. High exposures of oxygen can cause surface composition to change, as shown also by Table 1. This does not appear to take place upon adsorption at 105 or 300 K, but is slightly evident at 500 K. The effect of oxygen is that the Al content increases, while the Pd and Mn contents decrease. The trend is the same, but much more extreme, at 870 K, where the surface Al content goes from ca. 70 to 90%.

Exposure to oxygen also causes a new feature to emerge, adjacent to the low-energy Auger transition of metallic Al nominally at 68 eV. The new feature is known to be a useful chemical fingerprint. Reported by other workers at energies from 51 to 55 eV, it signals aluminum oxide, usually interpreted as Al_2O_3.[30, 33-35] The splitting between the metallic peak and the oxidic peak in our work is 11 eV, somewhat less than the splitting of 12-17 eV usually reported. This may indicate that the oxide is something different from stoichiometric Al_2O_3. (While it is known that high electron beam densities can reduce the oxide, our AES current densities are not sufficient to do so. Hence, any difference in stoichiometry cannot be attributed to this possible experimental artifact.[36]) The low-energy oxide peak grows in even at low temperature, showing that some oxidation occurs even at 105 K. The oxide peak becomes visible at exposures around 5-20 L, although the exact point at which it appears is

Figure 4. (a) Intensities of the metal Auger transitions as functions of oxygen exposure. The transitions are at 1396 eV for Al, 330 eV for Pd, and 589 eV for Mn. (b) Metal compositions (%) based upon data of part (a).

(a)
500 K
Pd
Mn
Al
870 K
Metal Auger Intensity, A.U.
Exposure of O2 (L)
(b)
500 K
Al
Pd
Mn
870 K
Metal Composition, %
Exposure of O2 (L)

somewhat obscured by overlap with the metallic peak at higher energy, and also with a weak metallic peak around 52-54 eV.[33, 34]

This overlap also prevents quantitative comparison of the amount of oxide or metal present under different conditions. However, a qualitative comparison can be made by evaluating the ratio of intensities, derived as illustrated in the inset to Fig. 5, and shown as a function of oxygen exposure for temperatures of 105-870 K in Fig. 5. This ratio should depend on the ratio of oxidic-to-metallic Al present in the near-surface region. Hence, the representation of the data in Fig. 5 shows clearly that the relative contribution of oxide is greater when oxygen exposure is carried out at 870 K, and (again) that oxidation proceeds quite similarly at the lower three temperatures.

Finally, AES can provide some other information about the aluminum oxide. First, the relative intensities of the AES transitions for oxygen and the main metallic component, Al, at 1396 eV, are revealing. Figure 1c shows that for our material, at oxygen saturation, the ratio of O/Al intensity is ca. 3.5:1. For Al_2O_3, under comparable conditions of measurement, the ratio is higher, 6:1.[30] Second, by assuming that the oxide layer forms a uniform skin at the surface, the attenuation of the metallic peak at 68 eV or the Pd transition at 270 eV can be used to estimate the thickness of the skin, which turns out to be in the range of 2-6 Å over the entire temperature range. Independent of the assumption of a uniform oxide layer, both of these calculations point toward the same broad conclusion: The quasicrystal ad/absorbs less oxygen than would be necessary to convert all of the surface and subsurface Al to stoichiometric Al_2O_3.

Figure 5. Ratios of oxide-to-metal Auger intensities, vs. oxygen exposure at different temperatures. The Auger transitions are the low-energy ones at 50-70 eV.

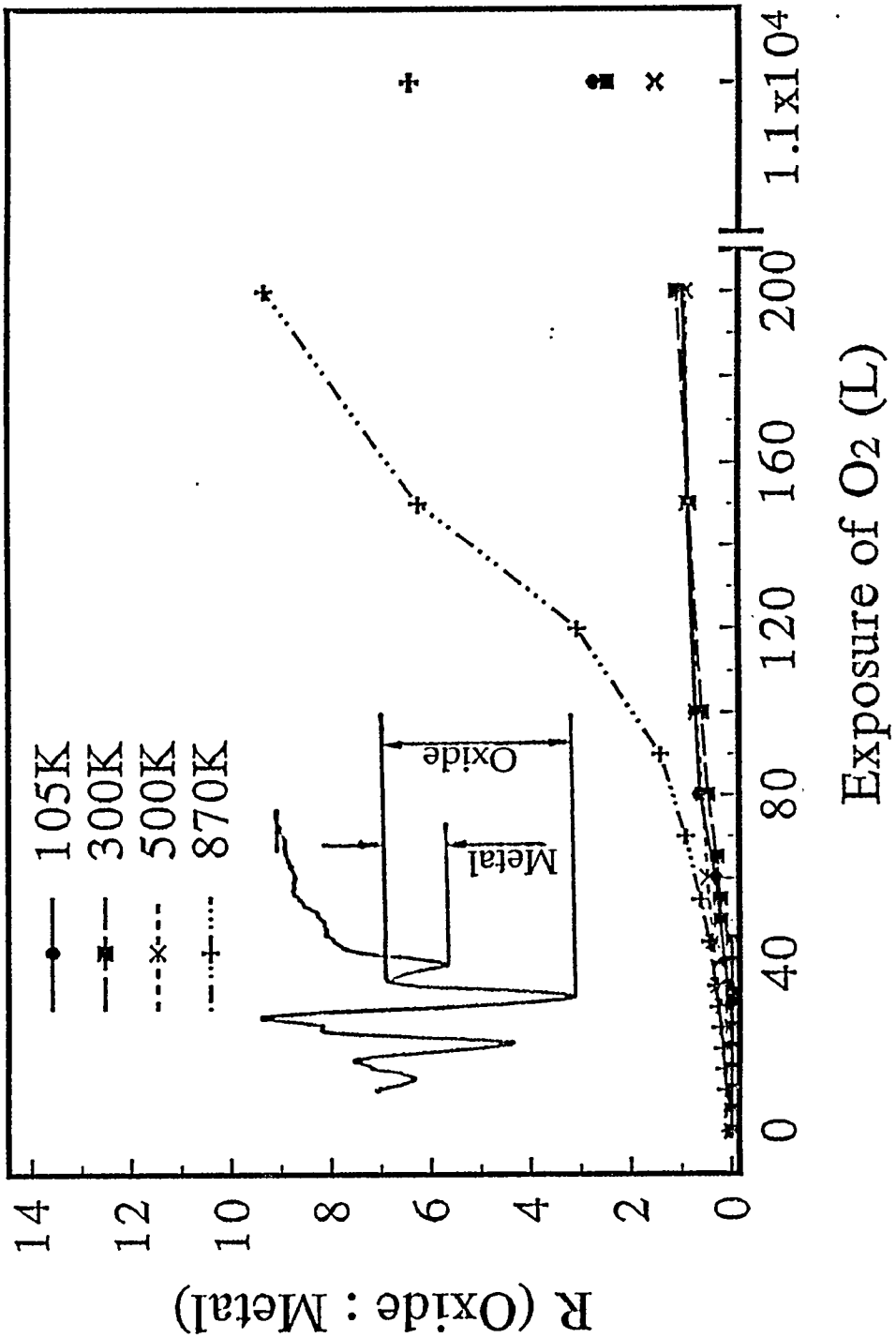
R (Oxide : Metal)
0
2
4
6
8
10
12
14
0
40
80
120
160
200
1.1x10^4
Exposure of O2 (L)
105K
300K
500K
870K
Oxide
Metal

Annealing the oxygen-saturated surface. Setting 870 K as an upper limit, we examine the effects of annealing an oxygen-saturated surface, using two probes. First, we monitor the AES oxygen signal intensity after slow annealing, and observe only a small decline (ca. 6%). Second, we monitor oxygen evolution with a quadrupole mass spectrometer, i.e. we perform thermal desorption spectroscopy (TDS). Oxygen desorption, probably from the large Ta sample holder, is observed immediately when heating begins, but not afterward. However, the design of the sample holder requires that a very slow heating rate be used in these experiments (1.1 K/s), which may decrease any desorption signal below the limit of detection. Nonetheless, the AES data confirm that most of the oxygen remains on the surface during annealing up to 870 K, i.e. the majority is neither lost to desorption nor to dissolution in the bulk. In summary, the oxygen layer is extremely stable upon annealing.

Effects of oxygen adsorption on surface structure. The effect of oxygen adsorption on surface structure is revealed by LEED. Figures 2c-d show LEED photos taken after exposures of 5 and 10 L at 105 K. Results are qualitatively the same at 300 and 500 K. No new superstructures form during oxygen adsorption. Instead, oxygen causes an attenuation of all diffraction spots and an increase in intensity of the diffuse background. Quantitative measurements of spot intensities during oxygen exposure reveal that all major diffraction spots decline in parallel. At oxygen saturation, the fivefold pattern is completely destroyed. Thus, oxygen has a major effect on the quasiperiodicity of the surface.

Changes in surface structure can be probed even more sensitively by measuring and comparing the I(E) curves of the diffraction spots at different stages during oxygen adsorption. These data are shown in Figures 6 (105 K), 7 (300 K), and 8 (500 K). Each figure contains six panels, a-f. Each panel shows data for a single, major diffraction spot, i.e. a ring-spot, and contains several I(E) curves. The top curve is always that for the clean surface, and curves with descending intensity are taken after 5, 10, and (sometimes) 15 L exposure. Hence, each panel contains data which correspond, at least, to the exposure sequence of Fig. 2a, c, and d. I(E) curves are not presented for oxygen exposures higher than 15L, since the dwindling spot intensity and rising diffuse background make the validity of such measurements uncertain.

As shown by Figures 6-8, major features in the I(E) curves are invariant with oxygen exposure. Some minor features do change, such as the peak at 115-120 eV which appears to shift downward in Fig. 8b, but since such changes do not occur systematically or frequently in the data, they are probably due to variation in background subtraction effects (cf. Section 2) with rising background intensity, and not due to real structural changes. Hence, oxygen adsorption does not cause gradual or continuous rearrangement of the areas of the crystal surface which exhibit five-fold periodicity; rather, these areas maintain their structure until the periodicity is simply destroyed. We expect that dissolution of oxygen would change the near-surface quasilattice constant, and should hence be recognizable in systematic shifts, at least, in the I(E) curves; the absence of such shifts thus

Figure 6. I(E) curves. In each panel, the top curve is for the clean surface and, in order of decreasing intensity, lower curves are for 5, 10, and (sometimes) 15 L exposure at 105 K.

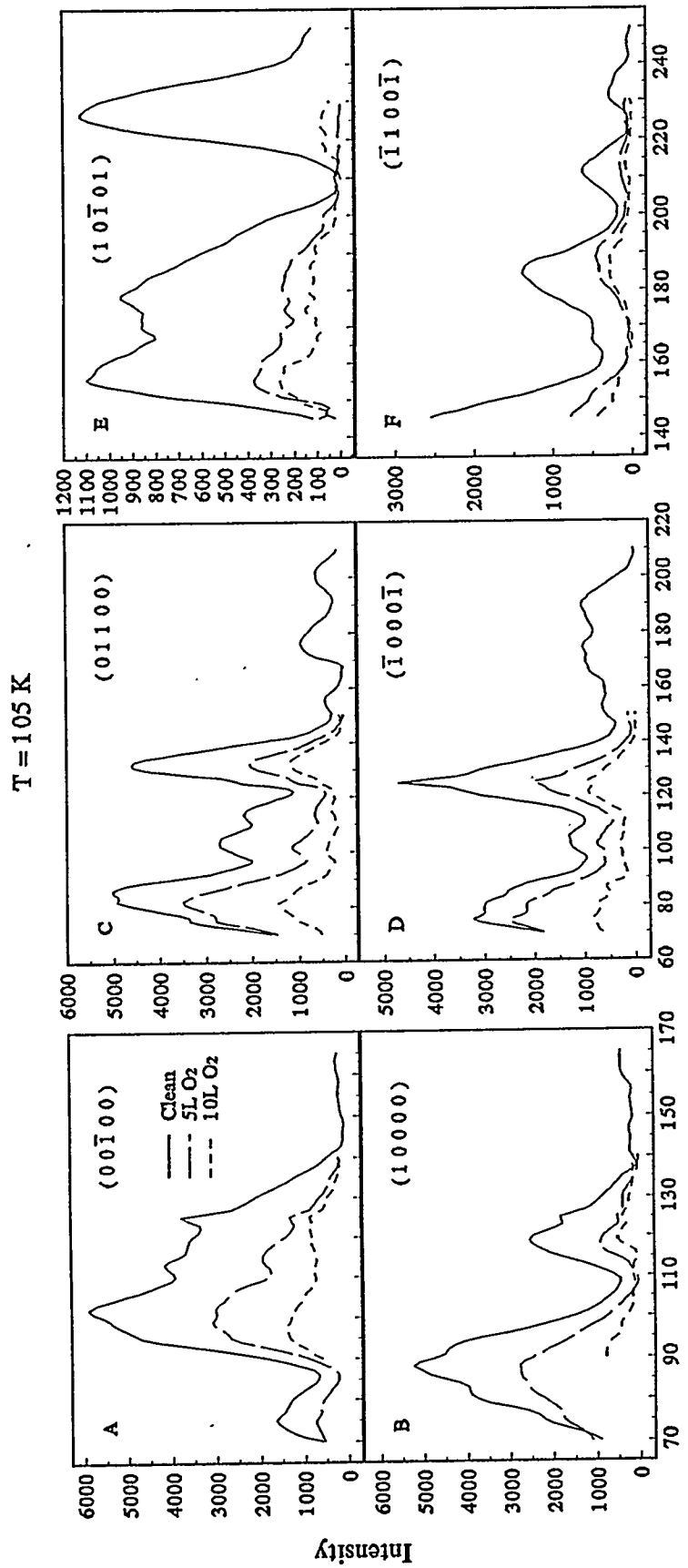
T = 105 K
Intensity
Beam Energy (eV)
A
(0 0 1̄ 0 0)
Clean
5L O2
10L O2
B
(1 0 0 0 0)
C
(0 1 1 0 0)
D
(1̄ 0 0 0 1̄)
E
(1 0 1̄ 0 1)
F
(1̄ 1 0 0 1̄)

Figure 7. I(E) curves. In each panel, the top curve is for the clean surface and, in order of decreasing intensity, lower curves are for 5, 10, and (sometimes) 15 L exposure at 300 K.

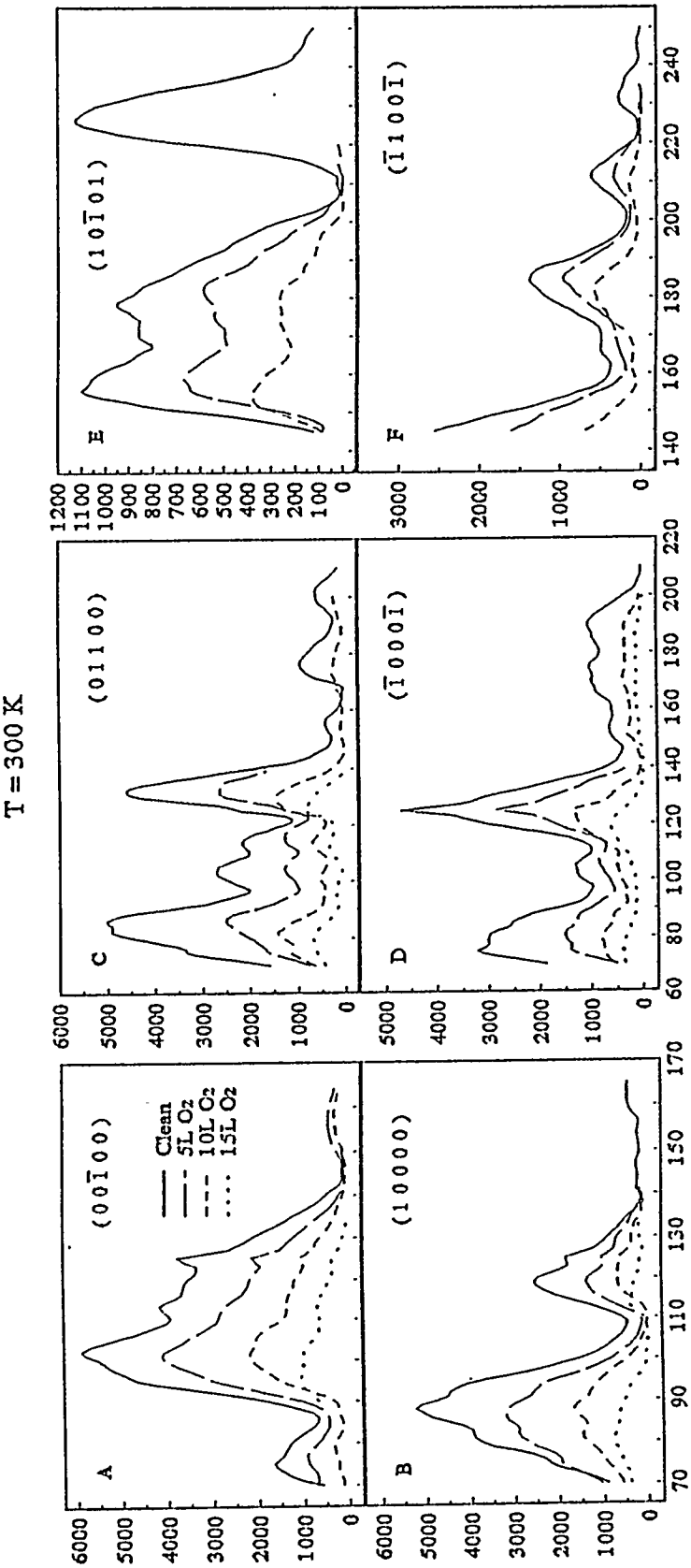
T = 300 K
A
(00$\bar{1}$00)
Clean
5L O2
10L O2
15L O2
B
(10000)
C
(01100)
D
($\bar{1}$000$\bar{1}$)
E
(10$\bar{1}$01)
F
($\bar{1}$100$\bar{1}$)
Beam Energy (eV)

Figure 8. I(E) curves. In each panel, the top curve is for the clean surface and, in order of decreasing intensity, lower curves are for 5, 10, and (sometimes) 15 L exposure at 500 K.

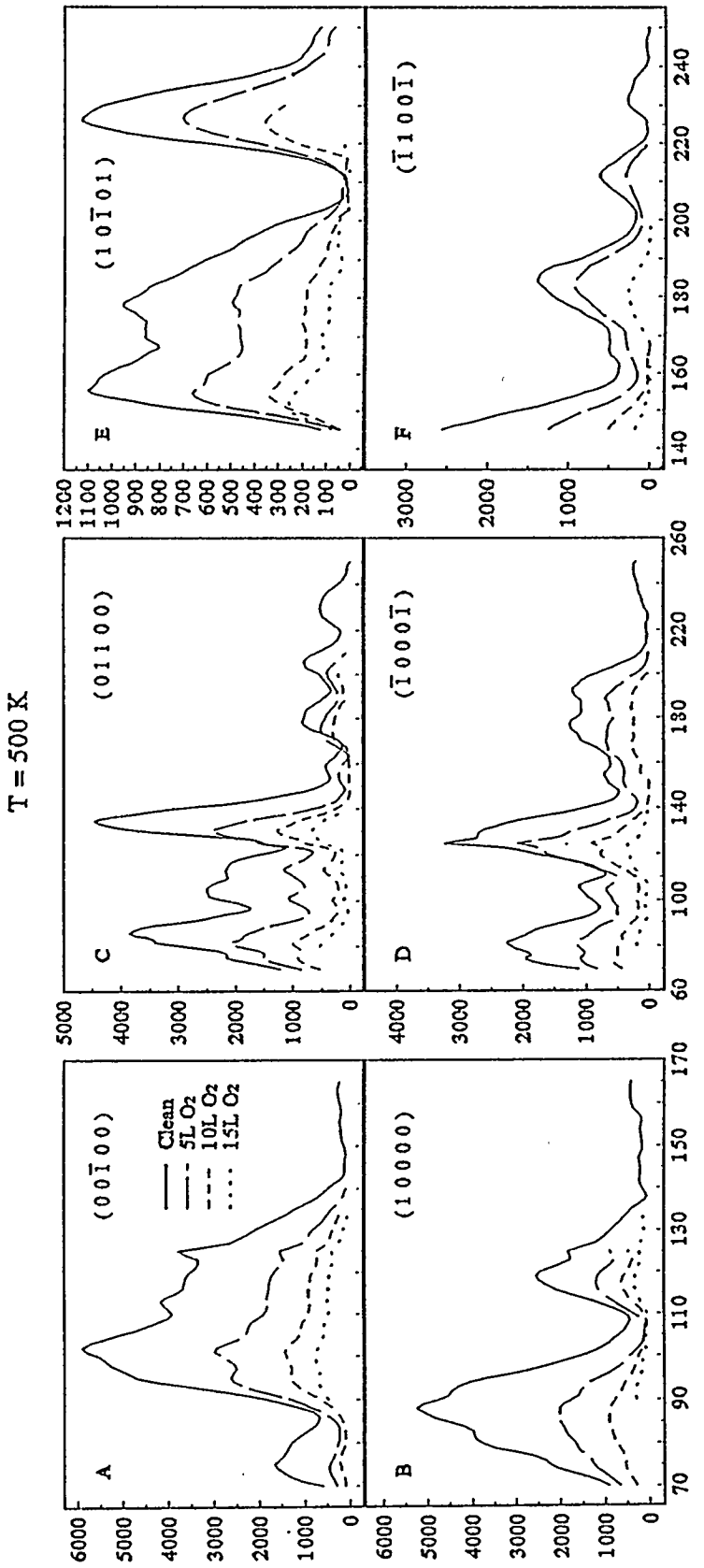
T = 500 K
A
(0 0 $\bar{1}$ 0 0)
Clean
5L O2
10L O2
15L O2
B
(1 0 0 0 0)
C
(0 1 1 0 0)
D
($\bar{1}$ 0 0 0 $\bar{1}$)
E
(1 0 $\bar{1}$ 0 1)
F
($\bar{1}$ 1 0 0 $\bar{1}$)
Beam Energy (eV)

suggests that there is not massive dissolution, at least not prior to destruction of the LEED pattern.

Finally, quantitative analysis of diffraction spot intensities as functions of oxygen exposure reveal that the exposure at which the LEED pattern disappears depends on temperature. Higher temperatures require higher exposures. This is shown in Fig. 9 by comparing data at 105 and 300 K, where the LEED intensity goes to zero at 12 and 20-25 L, respectively. Visual observation indicates disappearance at 500 K after 35 L, continuing the same pattern. An opposite trend exists in the exposures at which the Auger transition of aluminum oxide first becomes visible. The trends in both the LEED and AES data are shown in Fig. 10. (Recalling the problematic overlap between oxide and metal Auger peaks, the absolute values of the exposures for the Auger data in Fig. 10 are not too important, but the downward slope is certainly real.)

4. Discussion

As oxygen adsorbs on the $Al_{70}Pd_{21}Mn_9$ quasicrystal surface, it does not follow any of the usual sequence of events associated with oxidation of most transition-metal single crystals. Considering first the oxygen uptake curve (Fig. 3), we find that the only plateau in the curve is at saturation. In oxidation of some other pure transition metal surfaces, notably Ni, two plateaus are present; the first is thought to signal saturation of the chemisorbed layer and nucleation of the oxide, followed by rapid oxidation and (at the second plateau) saturation of a thin, multilayer oxide.[37, 38] The shapes of the curves in Fig. 3 provide no

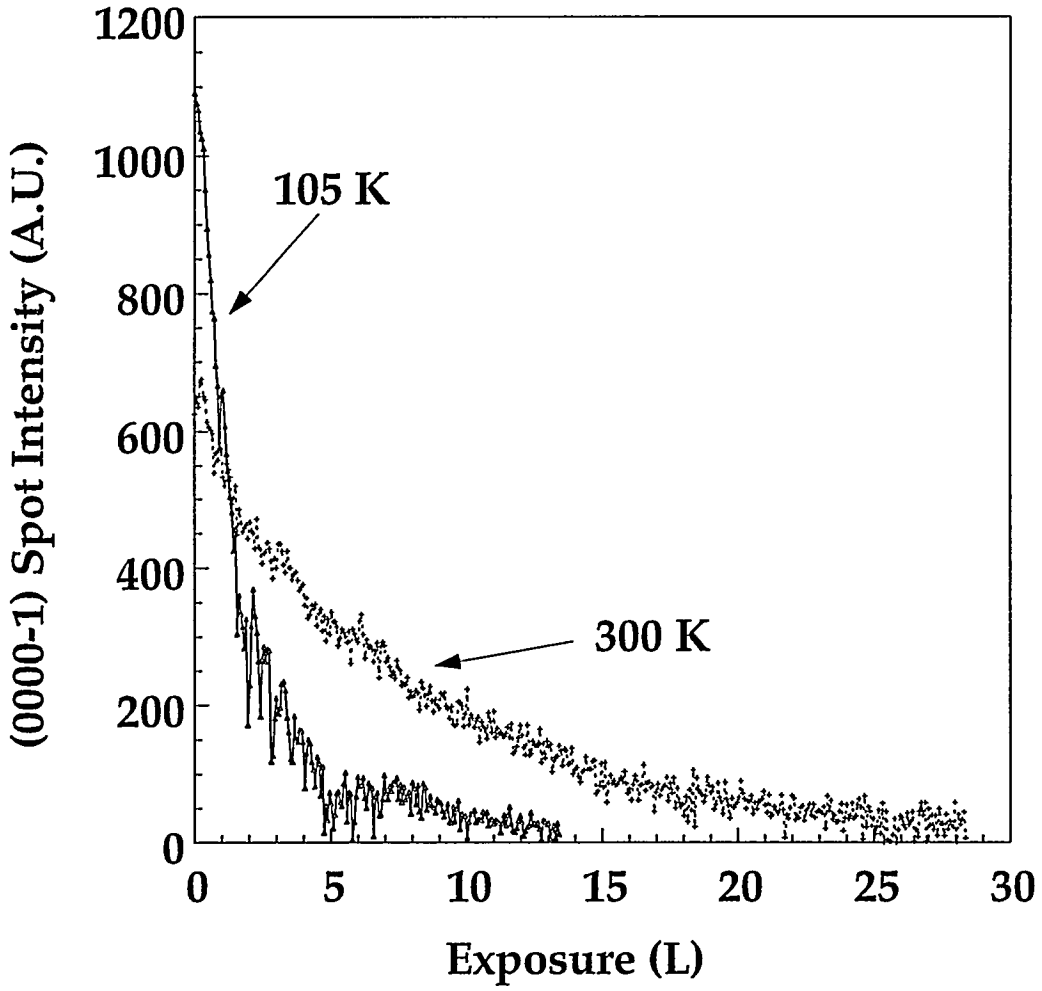

Figure 9. Intensity of a diffraction spot as a function of oxygen exposure at 105 and 300 K.

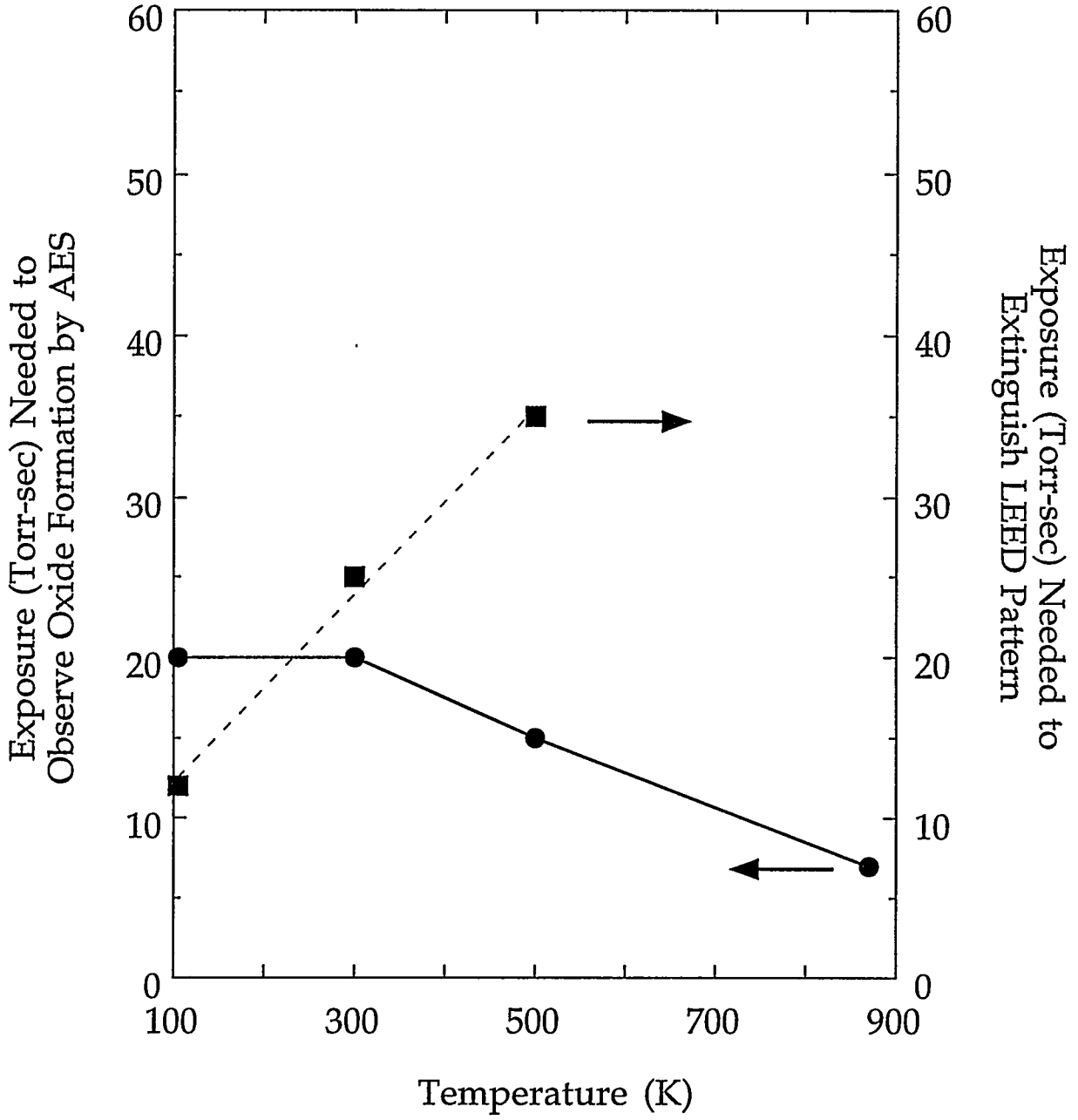

Figure 10. Point of appearance of the low-temperature Auger peak of Al oxide, and point of the five-fold LEED pattern, as functions of adsorption temperature.

evidence that this sequence is followed for the quasicrystal surface, at least for exposures up to 10^4 L, although this is not sufficient to rule out a nucleation mechanism for growth of the oxide-like layer. Considering next the effect of oxygen upon the LEED pattern, we find that oxygen does not produce new superlattice spots, indicating that there is no ordered, chemisorbed phase or ordered oxide-like overlayer, both of which form commonly on other transition metal surfaces.[38] Nor does oxygen dissolve significantly into the quasiperiodic regions of the crystal, since the I(E) curves are invariant during adsorption (Fig. 6-8). Oxygen does, however, have a massive impact on the quasicrystal structure, since adsorption eventually destroys the five-fold LEED pattern and produces a featureless, high background.

Does the LEED pattern disappear because of formation of surface oxide? The formation of an oxide of aluminum is clearly supported by AES at all temperatures, even down to 105 K. Whether oxides form for the other metals in the alloy, Pd and Mn, is not clear from the AES data alone. In principle, Mn should undergo a rather subtle change in AES lineshape upon oxidation[39] but, because Mn is present in such small amounts, we are unable either to confirm or exclude this effect. Oxidation, both of Al and Mn at the surface, would be thermodynamically reasonable, based upon values for heats of formation of bulk oxides: -1676 to -1657 kJ/mol for Al_2O_3, -1388 kJ/mol for Mn_3O_4, and -85 kJ/mol for PdO.[40]

The answer to the question is suggested by the data of Fig. 10, and the opposing trends shown therein. If the LEED pattern is destroyed by oxidation,

one would expect the exposure necessary for emergence of the aluminum oxide in AES and extinction of the LEED pattern to *both* increase, or decrease, as functions of temperature. However, the data of Fig. 10 show this not to be the case, and so this hypothesis is not viable. An alternative possibility is that the LEED pattern is destroyed by adsorption of a chemisorbed phase. At low temperatures, this phase would arrange most-randomly due to limited diffusion. (Temperatures in excess of 300 K, and as high as 700 K, are required to activate diffusion of atomic oxygen on Al surfaces.[41, 42]) Assuming that each atom disrupts the quasi-order in its immediate vicinity, such a random arrangement would extinguish the LEED pattern with maximum efficiency. As temperature increases, the chemisorbed phase could participate in activated processes, such as diffusion, leading to clustering and nucleation of the oxide. Thus, the LEED pattern would be destroyed less efficiently, but the oxide would be formed more efficiently, as temperature increases. This alternative hypothesis appears to be compatible with the experimental data. Thus, our data support the existence of a chemisorbed phase which is a precursor to oxidation, and which somehow destroys the quasiperiodicity of the substrate. Work on Al(100) has similarly indicated that the LEED pattern of the substrate fades during adsorption, not due to oxidation but rather due to random chemisorption.[35]

It is interesting to compare the oxygen adsorption properties of this quasicrystal with those of Al, because of the possibility that the properties of the quasicrystal are dictated simply by the properties of its major constituent. (We have already noted some similarities.) Adsorption of oxygen on Al(100)[35] and

Al(111)[43] produces no new LEED patterns, only attenuation of the pattern of the clean surface, which is very similar to the observations for the quasicrystal. Oxygen uptake curves, analogous to those of Fig. 3, and related data, have been published for Al(100)[34-36, 44-46] and Al(111).[33, 36, 42, 44, 47] While the shapes of the published curves are similar to ours, some differences exist. In general, the Al surfaces require much higher exposures to initiate formation of an oxide, and also much higher exposures to saturate the oxide overlayer. This may simply reflect a lower sticking coefficient on metallic Al than on the quasicrystal. Furthermore, the oxide is generally thought to be preceded by a chemisorbed phase on the aluminum surfaces, as on ours (although older papers on Al claimed oxide formation at all exposures, without a preceding chemisorbed layer[48]). For Al, it is also possible that the chemisorbed phase exists just below or coplanar with the surface Al layer.[48, 49] Our data do not preclude this possibility for the quasicrystal as well and may, in fact, be the reason why the chemisorbed layer can destroy the five-fold periodicity. Finally, the passivating oxide layer on Al is 4-8 Å thick, comparable to the thickness estimated for our system. It is also amorphous, which accounts for the fact that it produces no new superstructures in LEED.[48] In short, most of the oxidation characteristics of this Al-Pd-Mn surface are similar to those of the major constituent, Al, with the possible exception of the oxygen sticking coefficient.

Further information is available by returning to the temperature-dependence of oxidation. The major features of oxygen adsorption are very similar between 105 and 500 K, but rather different at 870 K. Upon going from

the lower temperatures to 870 K, the concentration of surface Al increases (Fig. 4), and the fraction of surface Al present as the oxide becomes much higher (Fig. 5). These data indicate, first, that oxygen induces surface enrichment in Al at 870 K. Second, surface segregation of Al is accompanied by enhanced oxidation of Al. Combining these two observations, we postulate that surface segregation of Al is driven by the fact that oxidation of Al is more exothermic than oxidation of Pd or Mn. (Preferential segregation of Al upon oxidation of mixed Al alloys is known also in other systems.[50, 51]) However, the system stops short of forming a *thick* surface layer in which *all* of the Al is present as Al_2O_3, even at 870 K; rather, a passivating layer forms which is rather thin (2-6 Å if completely uniform). There is also some indication, from AES line positions, that the oxide may differ chemically from Al_2O_3; we speculate that it is sub-stoichiometric.

Finally, one must ask why oxidation is enhanced at 870 K. For the (100) face of pure Al, oxidation is enhanced similarly by adsorption at 700 K.[35] There, limited oxidation at lower temperatures is attributed to the lack of mobility of the subsurface and surface oxygen atoms.[35, 41, 42] Another possibility, at least for the quasicrystal, is that the mobility of Al within the bulk lattice is so low at temperatures of 500 K or below, that it cannot migrate to the surface to form the enriched oxide layer. Other work suggests that the self-diffusivity of Mn in this material may be anomalously low.[52] Although self-diffusivity for the major constituents has not been measured, qualitative arguments can be made to suggest that self-diffusivity should be low for all components in a quasicrystal.[52]

5. Acknowledgments

We are indebted to T. Lograsso and D. Delaney for growing the single-grain quasicrystal sample, and to A.I. Goldman and S.W. Kycia for loaning us the cut, polished disk. We thank J. W. Anderegg for making the XPS measurements. We are also grateful for stimulating discussions with A.I. Goldman, S.W. Kycia, T. Lograsso, I. Anderson, and D. Sordelet. This work is supported by the Ames Laboratory, which is operated for the U.S. Department of Energy by Iowa State University under Contract No. W-7405-Eng-82.

References

[a]Permanent address: Department of Physics, Dong-A University, 840 Hadan 2-Dong, Saha-Gu, Pusan 604-714 South Korea.

1. D. Shechtman, I. Blech, D. Gratias and J. W. Cahn, *Phys. Rev. Lett.* **53** (1984) 1951.

2. D. R. Nelson, *Scientific American* **254** (1986) 43.

3. P. J. Steinhardt, *Science* **247** (1990) 1020.

4. P. W. Stephens and A. I. Goldman, *Scientific American* (April 1991) 24.

5. A. I. Goldman and M. Widom, *Ann. Rev. Phys. Chem.* **42** (1991) 685-729.

6. A. I. Goldman and K. F. Kelton, *Reviews of Modern Physics* **65** (1993) 213.

7. K. H. Kuo and S. Takeuchi, Eds., *Quasicrystals and Imperfectly Ordered Crystals*, vol. **150-151** (Trans Tech Publications, Switzerland, 1994).

8. A. M. Baro, R. Paganini and I. V. Rao, *J. Mater. Sci. Lett.* **8** (1989) 161.

9. E. G. McRae, R. A. Malic, T. H. Lalonde, F. A. Thiel, H. S. Chen and A. R. Kortan, *Phys. Rev. Letters* **65** (1990) 883.

10. A. R. Kortan, R. S. Becker, F. A. Thiel and H. S. Chen, *Phys. Rev. Letters* **64** (1990) 200.

11. T.-L. Ho, in *Quasicrystals: The State of the Art* D. P. DiVincenzo, and P. Steinhardt, Eds. vol. (World Publishing Co., 1991), p. 403-428.

12. A. R. Kortan, R. S. Becker, F. A. Thiel and H. S. Chen, in *Physics and Chemistry of Finite Systems: From Clusters to Crystals* P. Jena, and e. al., Eds. vol. I (Kluwer Academic Publishers, Netherlands, 1992), p. 29.

13. A. Sulyok, P. B. Barna and M. Menyhard, *Vacuum* **43** (1992) 477.

14. Z. Zhang, Y. C. Feng, D. B. Williams and K. H. Kuo, *Phil. Mag. B* **1993** (1993) 237.

15. T. M. Schaub, D. E. Bürgler, H.-J. Güntherodt and J. B. Suck, *Phys. Rev. Lett.* **73** (1994) 1255.

16. M. deBoissieu, M. Durand-Charre, P. Bastie, A. Carabelli, M. Boudard, M. Bessiere, S. Lefebvre, C. Janot and M. Audier, *Phil. Mag. Letters* **65** (1992) 147.

17. *Adv. Mat. and Processes* (1991) 6.

18. N. Rivier, *J. Non-Crystalline Solids* **153-4** (1993) 458.

19. J.-M. Dubois, S. S. Kang and Y. Massiani, *J. Non-Crystalline Solids* **153-4** (1993) 443.

20. J. M. Dubois, *Phys. Scripta* **T49A** (1993) 17.

21. J.-M. Dubois, S. S. Kang and A. Perrot, *Mat. Sci. Eng.* **A179/A180** (1994) 122.

22. J. M. Dubois, A. Proner, B. Bucaille, P. Cathonnet, C. Dong, V. Richard, A. Pianelli, Y. Massiani, S. Ait-Yaazza and E. Belin-Ferre, *Ann. Chim. Materiaux* **19** (1994) 3.

23. S. S. Kang, J. M. Dubois and J. Von Stebut, *J. Mater. Res.* **8** (1993) 2471.

24. M. Audier, M. Durand-Charre and M. DeBoissieu, *Phil. Mag. B* **68** (1993) 607.

25. S. Takeuchi, H. Akiyama, N. Naito, T. Shibuya, T. Hashimoto and K. Edagawa, *J. Non-Crystalline Solids* **153-4** (1993) 353.

26. C. Berger, E. Belin and D. Mayou, *Ann. Chim. Fr. Materiaux* **18** (1993) 485.

27. S.-L. Chang, J. W. Anderegg and P. A. Thiel, *J. Noncryst. Solids* (1995) submitted.

28. S. W. Kycia, A. I. Goldman, T. A. Lograsso, D. W. Delaney, D. Black, M. Sutton, E. Dufresne, R. Brüning and B. Rodricks, *Phys. Rev. B* **48** (1993) 3544.

29. O. L. Warren, Ph.D., Iowa State University (1993).

30. L. E. Davis, N. C. MacDonald, P. W. Palmberg, G. E. Riach and R. E. Weber, *Handbook of Auger Electron Spectroscopy*, (Physical Electronics Division, Perkin-Elmer Corporation, Eden Prairie, Minnesota, 1978).

31. M. V. Jaric, Ed., *Introduction to Quasicrystals* , vol. **1** (Academic Press, Inc., Boston, 1988).

32. C. Janot, *Quasicrystals: A Primer*, C. J. Humphreys, P. B. Hirsch, N. F. Mott, and R. J. Brook, Eds., Monographs on the Physics and Chemistry of Materials, vol. **48** (Clarendon Press, Oxford, 1992).

33. A. L. Testoni and P. C. Stair, *Surface Sci.* **171** (1986) L491.

34. A. Hoffman, T. Maniv and M. Folman, *Surface Sci.* **182** (1987) 56.

35. L. L. Lauderback and S. A. Larson, *Surface Sci.* **234** (1990) 135.

36. R. Michel, J. Gastaldi, C. Allasia, C. Jourdan and J. derrien, *Surf. Sci.* **95** (1980) 309.

37. W.-D. Wang, N. J. Wu and P. A. Thiel, *J. Chem. Phys.* **92** (1989) 2025.

38. C. R. Brundle and J. Q. Broughton, in *Chemisorption Systems* D. A. King, and D. P. Woodruff, Eds. vol. **3A** (Elsevier, Amsterdam, 1990), p. 131.

39. D. D. Sarma and P. Sen, *Proc. Indian Natn. Sci. Acad.* **49** (1983) 424.

40. D. W. Wagman, W. H. Evans, V. B. Parker, R. H. Schumm, I. Halow, S. M. Bailey, K. L. Churney and R. L. Nuttall, *J. Phys. Chem. Ref. Data* **11** (1982) Suppl. 2.

41. H. Brune, J. Wintterlin, R. J. Behm and G. Ertl, *Phys. Rev. Lett.* **68** (1992) 624.

42. H. Brune, J. Wintterlin, J. Trost, G. Ertl, J. Wiechers and R. J. Behm, *J. Chem. Phys.* **99** (1993) 2128.

43. F. Jona, *J. Phys. Chem. Solids* **28** (1967) 2155.

44. R. Michel, C. Jourdan, J. Castaldi and J. Derrien, *Surf. Sci.* **84** (1979) L509.

45. S. A. Larson and L. l. Lauderback, *Surf. Sci.* **234** (1991) 135.

46. S. A. Larson and L. L. Lauderback, *Surf. Ssci.* **284** (1993) 1.

47. F. Soria, V. Martinez, M. C. Munoz and J. L. Sacedon, *Phys. Rev. B* **24** (1981) 6926.

48. I. P. Batra and L. Kleinman, *J. Electron Spectr. Rel. Phenom.* **33** (1984) 175.

49. L. L. Lauderback, A. J. Lynn, C. J. Waltman and S. A. Larson, *Surf. Sci.* **243** (1991) 323.

50. J. Libuda, F. Winkelmann, M. Baumer, H.-J. Freund, T. Bertrams, H. Neddermeyer and K. Muller, *Surf. Sci.* **318** (1994) 61.

51. H. Graupnet, L. Hammer, K. Müller and D. M. Zehner, (1995) in preparation.

52. H. Nakajima, J. Asai, K. Nonaka, I. Shinbo, A. Tsai and T. Masumoto, *Phil. Mag. Lett.* **68** (1993) 315.

APPENDIX II

MOLECULAR BEAM EPITAXY SOURCE

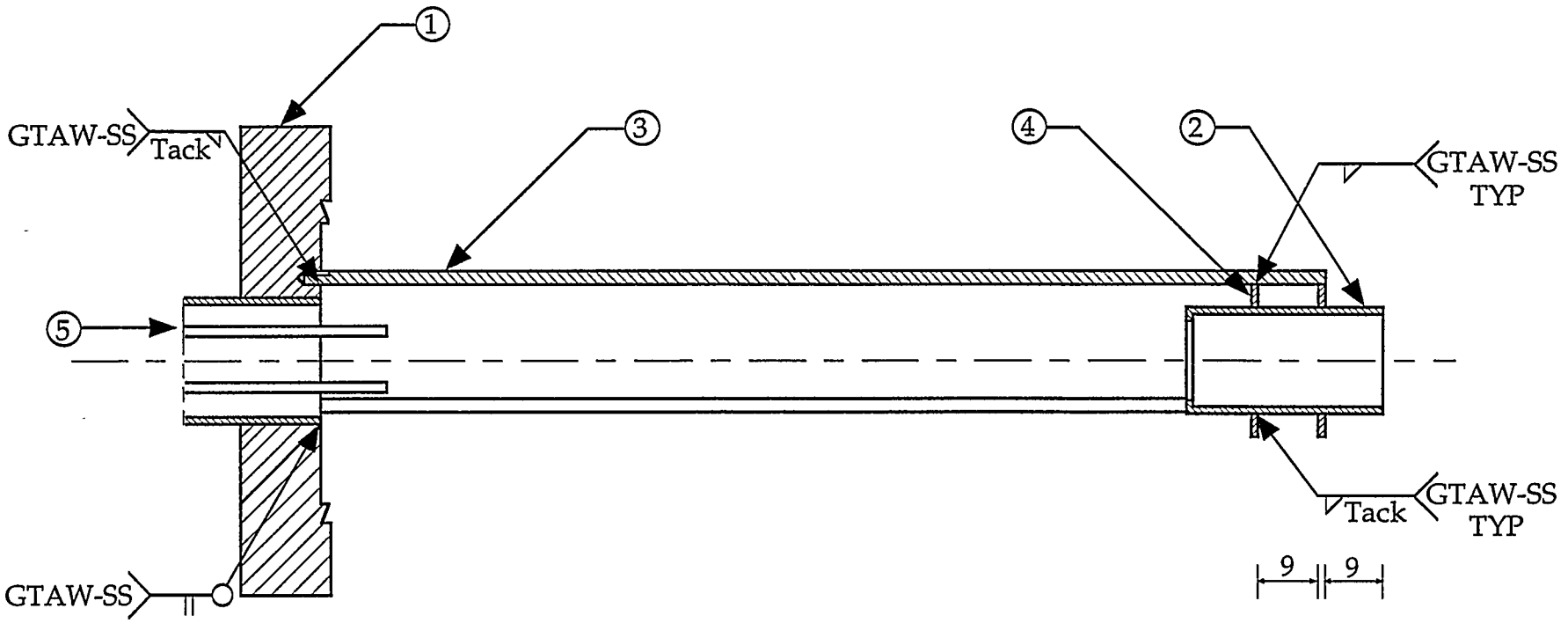

MBE Source

Full scale (mm)

Materials: Stainless Steel

All material used must be compatible with UHV (10^{-11} Torr).

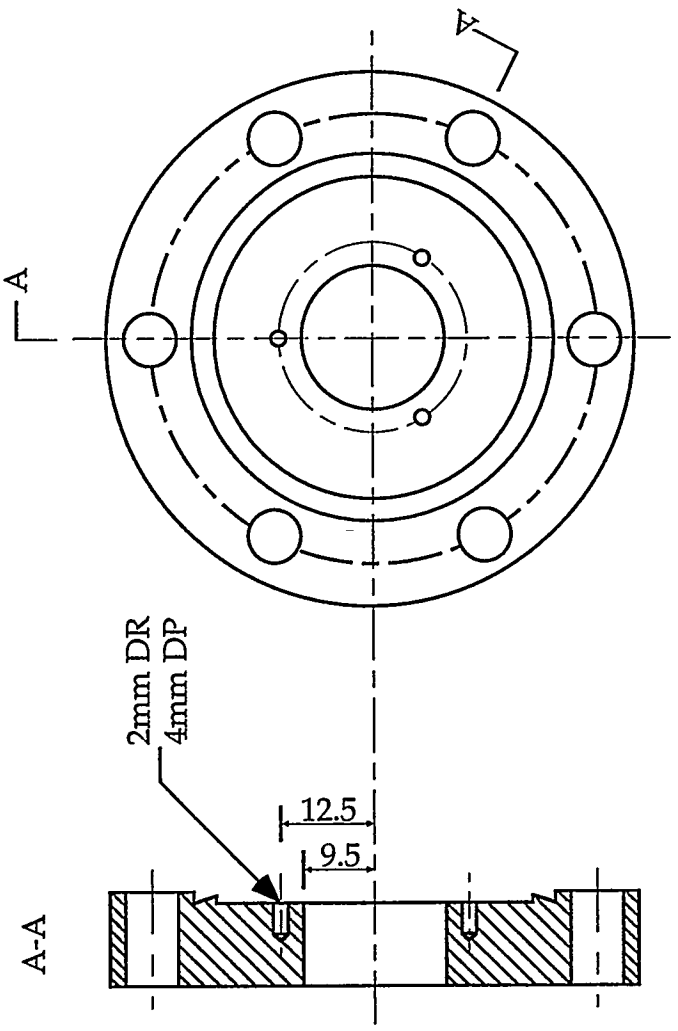

(1) Main flange. SS. Provided by requestor.

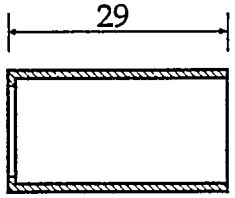

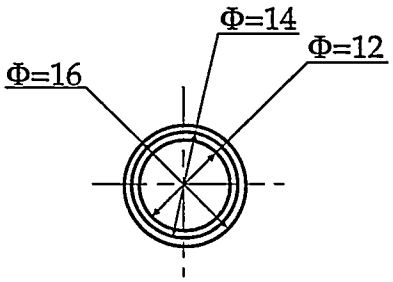

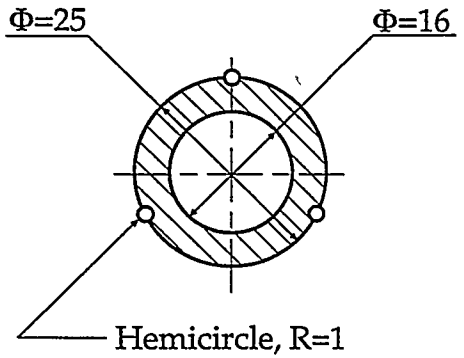

(2) Barrel: S.S., must be compatible with UHV.

(4) Supporting plate (1mm thick): S.S.

Must compatible with UHV.

Quantity: 2.

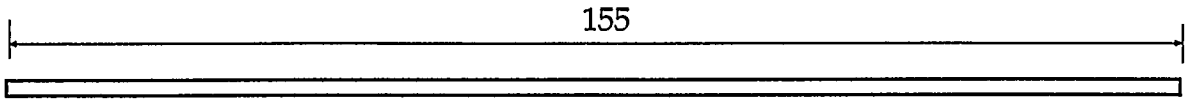

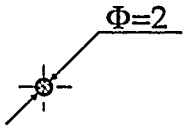

(3) Supporting rod: S.S., must compatible with UHV.

Quantity: 3.

(5) Electrical feedthrough: provided by requestor.

Note: All tolerance is ± 0.05mm

APPENDIX III

THE STM DATABASE

File name	Flux (ML/sec)	Coverage (ML)	Cluster Density x 10^{-5} (Å^2)	Leng. of time (min)	Observ. No.	Temp. (K)	Date	Note
Ag111695	1.635×10^{-3}	0.0327	2.143	449	18	295	Nov. 16, 1995	Crit. size
Ag112095	3.133×10^{-3}	0.03133	2.575	337	16	295	Nov. 20, 1995	Crit. size
Ag212095	3.300×10^{-3}	0.0330	2.740	242	11	295	Nov. 20, 1995	Crit. size
Ag112295	8.970×10^{-3}	0.04485	3.478	398	28	295	Nov. 22, 1995	Crit. size
Ag112695	1.570×10^{-2}	0.0314	3.830	677	29	295	Nov. 26, 1995	Crit. size
Ag113095	6.250×10^{-2}	0.1250	7.554	436	57	295	Nov. 30, 1995	Arrhenius
Ag120495	5.900×10^{-2}	0.1180	3.000	390	21	347	Dec. 04, 1995	Arrhenius
Ag120795	5.500×10^{-2}	0.1100	3.731	601	11	319	Dec. 07, 1995	Arrhenius
Ag121295	5.556×10^{-2}	1.0000*	n/a	790	22	295	Dec. 12, 1995	1 ML
Ag121995	5.624×10^{-2}	4.7800*	n/a	270	9	295	Dec. 19, 1995	5 ML
Ag122195	7.200×10^{-2}	0.1510	1.034	501	15	372	Dec. 21, 1995	Arrhenius

* Total coverage.